A ray-trace analysis of X-ray multilayer Laue lenses for nanometer focusing

H N Chapman[1,2,3] and S Bajt[3,4]

[1] Center for Free-Electron Laser Science, DESY, Notkestrasse 85, 22607 Hamburg, Germany

[2] Department of Physics, Universität Hamburg, Luruper Chaussee 149, 22761 Hamburg, Germany

[3] Hamburg Centre for Ultrafast Imaging, Luruper Chaussee 149, 22761 Hamburg, Germany

[4] DESY, Notkestrasse 85, 22607 Hamburg, Germany

E-mail: henry.chapman@desy.de

Abstract. Thick diffractive optical elements offer a promising way to achieve focusing or imaging at a resolution approaching 1 nm for X-ray wavelengths shorter than about 0.1 nm. Efficient focusing requires that these are fabricated with structures that vary in period and orientation so that rays obey Bragg's law over the entire lens aperture and give rise to constructive interference at the focus. Here the analysis method of ray-tracing of thick diffractive optical elements is applied to such lenses to optimise their designs and to investigate their operating and manufacturing tolerances. Expressions are provided of the fourth-order series expansions of the wavefront aberrations and transmissions of both axi-symmetric lenses and pairs of crossed lenses that each focuses in only one dimension like a cylindrical lens. We find that aplanatic zone-plate designs, whereby aberrations are corrected over a large field of view, can be achieved by axi-symmetric lenses but not the crossed lenses. We investigate the performance of 1 nm-resolution lenses with focal lengths of about 1 mm and show their fields of view are mainly limited by the acceptance angle of Bragg diffraction, and that aberrations can limit the performance of lenses with longer focal lengths. We apply the ray-tracing formalism for a tolerancing analysis of imperfect lenses and examine some strategies for the correction of their aberrations.

Keywords: diffractive optics, x-ray microscopy, geometrical optics

1. Introduction

Thick diffractive optical elements for X-ray wavelengths, including so-called sputter-sliced zone plates and multilayer Laue lenses (MLLs), are fabricated by depositing alternating layers of materials onto a substrate to achieve the required diameter or height of the lens, and then slicing the lens from this structure [1–3]. To date, imaging

resolutions of about 5 nm have been achieved [4,5]. Nanometer resolution requires layers of comparable or smaller period than the diffraction-limited spot size, positioned with high enough accuracy to avoid wavefront aberrations. At the wavelengths considered here—of about 0.1 nm and below—reasonable diffraction efficiency demands structures that are hundreds or thousands of times thicker (in the propagation direction) than the layer period and tilted to fulfil the Bragg condition of diffraction [1]. Such diffractive optical elements can be used as an objective lenses to construct various kinds of X-ray microscopes, including a transmission microscope where the lens forms a magnified image of an object on an area detector or a scanning transmission microscope where the lens creates a focused probe through which the object is scanned while mapping the transmission or emission of the sample. In all cases, an understanding of the imaging characteristics of the lens helps to optimise the design of the microscope and to specify its tolerances.

X-ray diffractive optical elements such as Fresnel zone plates and MLLs are usually designed according to ray-optics principles and often additionally analysed in the framework of wave optics calculations, dynamical diffraction, or coupled-wave theories to model the performance at one or several field points [6–10]. Ray-tracing allows rapid and accurate analysis of complex geometries over extensive parameter spaces, and can be used as a computational engine for optimisation of particular parameters in a design. Such an analysis is used in the optical industry for the design of instruments such as telescopes, microscopes, and micro-lithography systems, where optimal optical performance is paramount. Ray tracing has long been applied to model Fresnel zone plates, giving insights into aplanatic designs, for example [11–14]. The modelling of diffractive optical elements in complex optical systems has been well established, with the development of holographic optical elements to produce arbitrary wavefronts abetted by the rise of computational ray-tracing methods and software [15–21]. Some of these principles have been recently rediscovered for the analysis of meta-lenses [22,23], and we use them here for a comprehensive study of MLLs for nanometer focusing. We consider both axi-symmetric lenses formed by depositing layers onto a cylindrical substrate, for example, as well as lenses that focus only in one direction, created by deposition onto a flat substrate.

Achieving a resolution of 1 nm is certainly a challenge from the points of view of lens fabrication and instrumentation stability, but it appears that the concepts and technologies to achieve this are in hand. Layer periods below 1 nm have been demonstrated [24] and methods to produce lenses with tilted layers—required for rays to satisfy the Bragg condition throughout the lens pupil—have been developed [25]. A recent theoretical and experimental analysis of crossed 1D MLLs has pointed out the stringent requirements to align the lenses with respect to each other [9]. Here we characterise the field-dependent aberrations of axi-symmetric and 1D MLLs formed on flat and curved surfaces, using ray-tracing methods established for thick holographic optical elements (HOEs) in which the phase profile (caused by additional wavelength of path of each "fringe" or period in the structure) is combined with a "modified

Snell's law" [18] that redirects rays by Bragg diffraction. We find that curving the lenses provides useful extra degrees of freedom in the optical design, but for small focal lengths (giving diameters of lenses that can be reasonably fabricated) the fields of view are limited by the rocking-curve width of Bragg diffraction. The ray-tracing approach is reviewed in section 2 and further expanded in section 3 for X-ray MLLs. Fourth-order expressions of the wavefront aberrations are derived in sections 4 and 5 and exact computations presented for lens systems with 1 nm resolution. Finally, some tolerances for the fabrication of MLLs are given in section 6. The symbols used in this paper are listed in table 1 for convenience.

2. MLLs as holographic optical elements

A perfect focusing lens transforms the wavefront $\phi(\boldsymbol{r})$ of an incoming plane wave into a converging spherical wave such that at each point a ray, defined by the normal of ϕ, is deflected towards a common point on the optic axis. The deflection $\sin 2\theta(\boldsymbol{r}) = -\lambda/2\pi \nabla\phi(\boldsymbol{r})$ must therefore increase with distance $r = |\boldsymbol{r}|$ from the optic axis, for a wavelength λ. In a refractive lens, deflection is caused by refraction and the change in deflection is achieved with a variation of the direction of the surface normal with position—that is, with a curved surface. In diffractive optics, deflection is caused by diffraction. Rays no longer traverse the path of least time to arrive at the focus, but instead accrue extra path-lengths of integral multiple wavelengths to constructively interfere.

Conceptually, a diffractive lens that focuses an incoming plane wave (i.e. rays from a point source located at infinity) to a point a distance f from the lens can be formed holographically by interfering that plane wave with a spherical wave emanating back towards the lens from the focus. For a cylindrical coordinate system (r, z), the phase of the resultant interfering field is thus the difference of the "reference" plane wave phase $\phi_r = -kz$ and the "object" spherical wave phase, $\phi_o = k[r^2 + (z - f)^2]^{1/2}$, with $k = 2\pi/\lambda$. The phase field $\bar{\phi}(r, z) = \phi_o - \phi_r$ gives surfaces at constant $\bar{\phi}(r, z)$ on which the incident and deflected rays sum to a constant path length. The family of surfaces at $\bar{\phi}(r, z) = kf + 2\pi n$, where n is an integer, provide the form of a diffracting structure that can be fabricated on a surface specified by $z = s(r)$. Rays deflected by such structures will constructively interfere at the focus. The family of curves may be written as

$$z + \sqrt{r^2 + (z - f)^2} = f + n\lambda, \tag{1}$$

which can be expanded and simplified to an expression describing a set of paraboloids

$$r_n^2 = 2n\lambda \left(f + \frac{n\lambda}{2} - z \right) \tag{2}$$

that are illustrated in figure 1. For example, the flat diffractive lens formed at $z = s(r) = 0$ reproduces the Fresnel zone plate formula with bi-layer zones separated at radii r_n.

Table 1. List of symbols and their meanings.

x, y, z	Cartesian coordinates of ray positions in the lens with the origin at the lens vertex
r, ψ, z	Cylindrical coordinates of ray positions
x_1, y_1; x_2, y_2	Coordinates of rays in the first and second lenses (for a crossed pair of 1D lenses)
ρ, ρ_x, ρ_y	Angular pupil coordinates, $= r/f$, x/f, y/f
x_i, y_i	Image-plane coordinates
λ	X-ray wavelength as assumed in the design of the lens
λ_m; $\Delta\lambda$	X-ray wavelength of a measurement; $\Delta\lambda = \lambda_m - \lambda$
k	Wavenumber, $= \lambda/(2\pi)$
f; f_1, f_2	Designed focal length of the lens; focal lengths of the first and second lenses
f_m	Focal length of the lens at the measurement wavelength, $= f\lambda/\lambda_m$
a, b	Distances from the lens to the object and image, both positive for a real image
α_x, α_y	Field angles in the x and y directions
NA	Numerical aperture
δ	Imaging resolution, $= 0.66\lambda/\mathrm{NA}$ for a circular pupil and $0.5\lambda/\mathrm{NA}$ for a square pupil
D	Lens diameter, $= 2\mathrm{NA}f$
τ	Thickness of the lens (in the direction parallel to the optic axis)
R; R_1, R_2	Radius of curvature of the lens surface; radii of curvature of the first and second lenses. Positive for surfaces that are convex as seen from the field at infinity.
$s(r)$	Sag of the lens surface in the z direction
$\boldsymbol{s}$	Vector from the vertex to the ray intersection with the surface of the lens
$\hat{\boldsymbol{n}}$	Normal of the surface of the lens
ϕ_r, ϕ_o	Reference-wave and object-wave phases used in the construction of a HOE
$\bar{\phi}$	Holographic phase field, $= \phi_o - \phi_r$
ϕ; ϕ_1, ϕ_2	Phase imparted by the lens onto the reference-wave beam (2π per layer period); phases for the first and second lenses
ϕ_m	Phase imparted by the as-manufactured lens onto the reference-wave beam (2π per layer period)
θ	Bragg angle, with a deflection angle given by 2θ
$\Delta\theta$	Deviation of a ray from the Bragg angle
r_n; $r_{n(m)}$	Radial position of the n^{th} layer pair from the optic axis; ditto for the as-manufactured lens
$d(r)$; d_n	Layer period at a position r in the lens; period of the n^{th} layer pair
C	Intersection point of planar or conical layers that approximate the holographic phase field $\bar{\phi}$
$\boldsymbol{q}$	Reciprocal-space vector with a magnitude $1/d$ and direction normal to the layers
$\boldsymbol{k}_{\mathrm{in}}$, $\boldsymbol{k}_{\mathrm{out}}$	Wave-vectors of the incident and diffracted rays
$\boldsymbol{r}$, $\boldsymbol{r}'$	Normal vectors of the incident and diffracted rays
l_1, l_2, l_{12}	Lengths of rays traced from the incident wavefront to the (first) lens, from the (second) lens to the image plane, and between the lenses
OPL	Optical path length
OPD	Optical path difference
$\mathrm{OPD}^{(4)}$; $\mathrm{OPD}_{\mathrm{SA}}$	Fourth-order series expansion of the OPD; OPD due to spherical aberration
I_L	Efficiency of Bragg diffraction as a function of the deviation from the Bragg condition
Γ_L	Pendellosung period for dynamical diffraction. Maximum diffraction efficiency is obtained for $\tau = \Gamma_L/2$.
ϵ; ϵ_m	Deviation parameter for rays (equal to zero when the Bragg condition is satisfied); deviation parameter for the as-manufactured lens.
w_ϵ, w_θ	Width of the diffraction rocking curve in terms of ϵ; in terms of $\Delta\theta$.
η	Dimensionless parameter, $= \epsilon/w_\epsilon = \Delta\theta/w_\theta$
$\delta_1 - \delta_2$	Difference of the optical constants of the two materials of the multilayer, $= 6.7 \times 10^{-6}$ for SiC/WC at a wavelength of 0.075 nm
χ_x, χ_y, χ_z	Rotations of the second lens relative to the first, about the x, y, and z axis
h	Scale factor of the lens
p	Deposition rate of material in the fabrication of the MLL
$c(t)$; c_1	Drift of the deposition rate with time; coefficient of linear drift
β	Relative change in deposition rate per unit length of material deposited, $= c_1/p$
Δd	Offset error in the bi-layer period d
γ	Inclination of the surface normal of a MLL relative to the optic axis

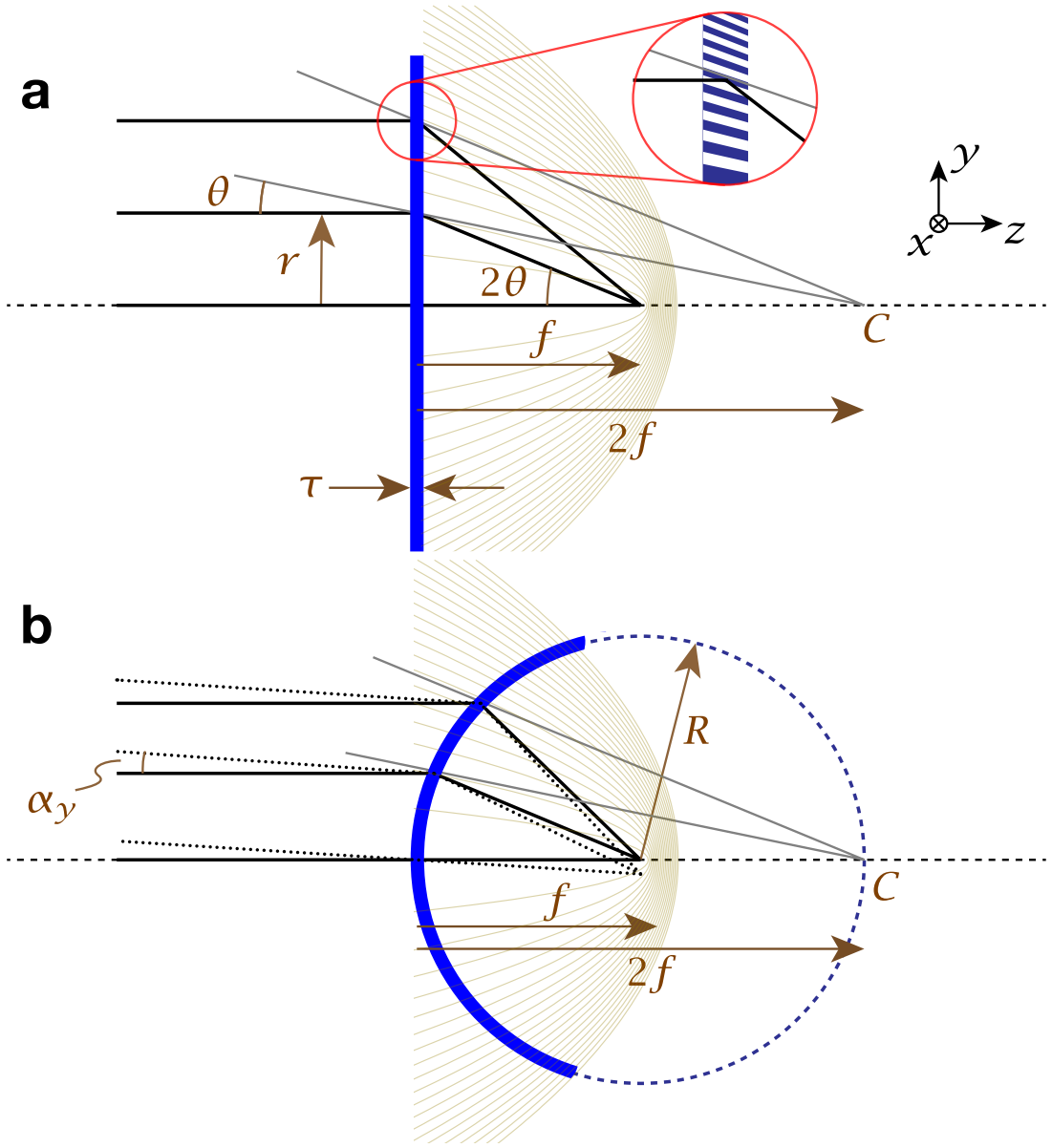

Figure 1. Schematic diagrams of focusing by a flat (a) and a curved (b) multilayer Laue lens. The lens of thickness τ is depicted in blue and consists of layers whose surfaces (seen in the inset) follow a family of paraboloids shown in brown and which can be approximated as planes or cones that intersect at the point C, located a distance $2f$ from the lens. The radius of the lens is R, equal to infinity in (a) and to f in (b). Off-axis rays at an angle α_y are shown as dotted lines.

The phase imparted on the incident plane wave (replicating the reference wave) by the diffracting structure fabricated on the surface $s(r)$ is given by

$$\begin{aligned}\phi(r) &= \bar{\phi}(r, s(r)) - \frac{2\pi f}{\lambda} \\ &= \frac{2\pi}{\lambda}\left(s(r) + \sqrt{r^2 + \left(f - s(r)\right)^2} - f\right),\end{aligned} \tag{3}$$

such that $\phi(0) = 0$. Since each period in a diffracting structure adds an additional 2π of phase to the wave, the number of periods from the optic axis to the point r on the surface is $n = \phi(r)/(2\pi)$. The change in ray direction caused by the diffracting structure is given by the vector phase gradient $-\lambda/2\pi\nabla\phi$, which can be computed from equation (3) as [19]

$$\begin{aligned}\frac{\lambda}{2\pi}\frac{\partial\phi}{\partial r} &= \frac{\lambda}{2\pi}\left(\frac{\partial\bar{\phi}}{\partial r} + \frac{\partial\bar{\phi}}{\partial s}\frac{\partial s}{\partial r}\right) \\ &= \frac{r}{\sqrt{r^2 + (f-s)^2}} + \frac{\partial s}{\partial r}\left(1 - \frac{f-s}{\sqrt{r^2 + (f-s)^2}}\right) \\ &= \sin 2\theta + 2\frac{\partial s}{\partial r}\sin^2\theta,\end{aligned} \tag{4}$$

where 2θ is the deflection angle as shown in figure 1. For a flat lens ($s(r) = 0$), we find that

$$\frac{\lambda}{2\pi}\frac{\partial\phi}{\partial r} = \sin 2\theta = \frac{\lambda\cos\theta}{d(r)}. \tag{5}$$

Here we have considered X-rays interacting with three-dimensional diffracting structures, where a deflection by 2θ is attained by a structure that modulates in density in one direction by a period d satisfying Bragg's law, $\lambda = 2d\sin\theta$. This gives the equality to the final term in (5), from which an expression for $d(r)$ can be obtained. Efficient diffraction requires that the direction of the modulation be parallel to the momentum transfer, equal to the difference of the wave-vectors of the rays, $\mathbf{k}_{\text{out}} - \mathbf{k}_{\text{in}}$, for a wave-vector of the incident ray given by $\mathbf{k}_{\text{in}}$ and the outgoing wave-vector $\mathbf{k}_{\text{out}}$. This is equivalent to the rays reflecting from the "layers" of constant density in the structure, oriented at an angle θ to the z axis. Indeed, (5) indicates that the gradient of phase (in the transverse direction r) is inversely proportional to the separation of layers in the r direction, $d(r)/\cos\theta$, for their minimal separation $d(r)$ in the direction normal to the layers. This would be equal to the deposited height of layers (ie. their thickness in the direction normal to the substrate they are deposited onto) which should thus follow the recipe of

$$\frac{d(r)}{\cos\theta} = \frac{\lambda f}{r}\sqrt{1 + \frac{r^2}{f^2}} \approx \frac{\lambda f}{r}\left(1 + \frac{r^2}{2f^2}\right). \tag{6}$$

Here, we have assumed that the period d is well defined at any point r along the height of the lens, which is to say that the period changes slowly compared to r, or $|\partial d/\partial r| \ll 1$. Taking the leading term in the approximation in (6), this is equivalent to $d \ll r$.

The optical performance of diffractive optics have long been modelled in this fashion, in which a phase function $\phi(r)$ on a surface $s(r)$ defines a structure with periods that vary as $d(r)$. These functions can then be used in a computational ray-tracing procedure to deflect rays according to $\nabla\phi(r)$, as a modified Snell's law [18]. When the structure is fabricated not through interference of waves as a traditional HOE, but rather as a "computer-generated hologram" or "meta-lens" such as by lithography or multilayer deposition, we must contend with the fact that the structure might differ from the ideal. Furthermore, we are interested in understanding off-axis aberrations and conditions where Bragg diffraction, for example, is not strictly satisfied. An established method to treat these cases is to use the structural properties of the lens such as the local layer period $d(r)$ to prescribe the path of a ray, taking into account the accrued phase $\phi(r)$ due to the number of diffracting periods in the structure. The wavefront aberration is calculated by tracing many such rays throughout the pupil of the optical system, from which a wave-optical calculation can be made to determine imaging characteristics such as the point spread function, or to express the form and magnitude of particular aberrations. There are some approximations in this approach, such as the assumption that locally, the diffracting structure acts as a grating of a single period. More accurate treatments utilise dynamic diffraction of strained crystals [7], the multislice algorithm [26], or coupled-wave numerical modelling [8].

3. Analysis of multilayer Laue lenses

3.1. Design of a multilayer Laue lens

X-ray multilayer Laue lenses (MLLs) can be considered as thick diffractive optical elements, in which diffraction occurs as a volume effect. Efficient diffraction is obtained by satisfying the Bragg condition as mentioned above, which requires the layers to be tilted by θ, half the deflection angle. MLLs are fabricated by the alternating deposition of two (or more) materials onto a substrate followed by slicing to produce a structure similar to that illustrated in the inset of figure 1 (a). The variation of period $d(r)$ throughout the lens is controlled by varying the amount of material deposited in each layer (e.g. by changing the time the substrate is exposed to each sputtering target) and the required tilt can be obtained by placing a mask edge between the sputtering target and the substrate [25]. MLLs provide high efficiencies for X-ray energies above about 10 keV (wavelengths less than about 0.1 nm) with periods typically in the range of 1 nm to 100 nm. The optimum thickness τ of the lens that the X-rays transmit through is half the so-called Pendellösung period Λ_L, which can vary from several micrometers at lower X-ray energies to many tens of micrometers at harder energies, depending on the materials and (weakly) on the period.

X-ray MLLs are usually fabricated as flat lenses with bi-layers (periods) positioned according to the Fresnel zone plate condition of (2) with $z = 0$. Given the large thickness τ of an MLL, rays can be thought to reflect not only on the front surface of the structure

but at points some distance z into the interior of the MLL. In order that these rays are directed to a common focal point the layers should follow the paraboloids given by (2). The approximation of the paraboloids to cones (or tilted wedged layers for one-dimensional focusing) can be found from a Taylor series of $r_n(z)$, showing the gradient of each layer is approximately $r_n/(2f)$, which is indeed equivalent to the angle $\theta(r)$ of layers mentioned above and shown in figure 1. Also, given a bi-layer thickness $d_n = r_{n+1} - r_n$ it can be shown that $d_n^2 \approx f\lambda/(4(n+1/2))$, and from (2) it follows that $d_n \approx f\lambda/r_n$. For the purpose of ray tracing, the phase imparted to the ray that intersects the lens at a position r, equal to $2\pi n$, is given by $\phi(r)$ of (3).

3.2. Ray tracing of MLLs

We first consider the ray-trace analysis of perfect MLLs that are designed to deflect incident parallel rays to the focal point. In section 6 we consider lenses with imperfections (due to manufacturing processes, for example) where $\phi(r)$ must be modified due to deviations in $d(r)$ from the ideal. Generally, ray tracing tracks a ray from a particular point in an object, via straight-line propagation through homogeneous space to an interface where it is refracted (according to Snell's law) or diffracted (according to a grating equation or Bragg's law) before propagating to the next interface, and so on, until the plane of interest is reached [18]. Unlike a more complete calculation that may utilise Huygens wavelets formed at each scattering point of the structure (such as used in a multislice calculation [26]), a ray described by the unit vector $\hat{\boldsymbol{r}}$ incident upon a diffractive optic is taken to follow a single trajectory only. As mentioned above, the direction of the diffracted ray $\hat{\boldsymbol{r}}'$ is set by Bragg's law, cast here as $(2\pi/\lambda_m)\hat{\boldsymbol{r}}' = \boldsymbol{k}_{\rm out} = \boldsymbol{k}_{\rm in} + \boldsymbol{q}$ for an incident wave-vector $\boldsymbol{k}_{\rm in} = (2\pi/\lambda_m)\hat{\boldsymbol{r}}$ (see figure 2 (a)). That is, the ray has a "measurement" wavelength λ_m which may differ from the parameter λ used in the design of the diffracting structure that modulates with a period $d = 2\pi/|\boldsymbol{q}|$ in the direction of $\boldsymbol{q}$. This presumes that the diffracting structure will indeed be oriented in the Bragg condition. For thin structures, or to account for diffraction of a ray in an off-Bragg condition (whether that be due to an angular deviation or a change in wavelength), it can be assumed that the termination of the periodic structure by the surface leads to truncation rods in reciprocal space that extend from $\boldsymbol{q}$ along the direction of the surface normal $\hat{\boldsymbol{n}}$, in which case the "refraction" of the single ray can be described as

$$\hat{\boldsymbol{r}}' = \hat{\boldsymbol{r}} + \frac{\lambda_m}{2\pi}\boldsymbol{q} + \epsilon\hat{\boldsymbol{n}}, \tag{7}$$

where the deviation parameter ϵ is chosen to ensure that $|\hat{\boldsymbol{r}}'| = 1$, and $\boldsymbol{q}$ points towards the optical axis (rather than away from it) for a focussing optic. Although (7) was derived in the context of the geometric theory of diffraction (see Chapter 3.3 of [27]) the expression also holds in the framework of dynamical diffraction theory (see Chapter 4.8.5 of [27]). A similar approach used in the ray-tracing of thick HOEs is referred to as the blurred grating vector approach [28]

As the ray is traced sequentially from interface to interface, the optical path length (OPL) of the ray is accumulated. In a perfect imaging system based on refractive optics, rays originating from a point in the object plane should all accumulate the same optical path (proportional to the flight time) upon their intersection of the image plane at the image point. A map of the differences of the optical path lengths of the rays to that of a reference ray (optical path difference, OPD), as a function of the pupil coordinates of the rays, gives the map of the wavefront aberration. This aberration can be related to the point spread function of the lens through a wave optic calculation, treating the aberration as a phase error [29]. In a diffractive optic such as an MLL, however, rays reflecting from each subsequent bi-layer accrue an extra wavelength of path-length, for a total path difference of $n\,\lambda_m$ for n periods, or a phase of $2\pi n$. For a wavelength equal to the design wavelength, $\lambda_m = \lambda$, this phase is exactly $-\phi(r)$ as provided by the diffracting structure. The formation of the image is dictated by the constructive interference of waves at the measurement plane rather than the principle of least time. The lag of rays by a wavelength per period of the structure is thus not apparent and it is accounted for by forming the OPD as [18]

$$\mathrm{OPD}(r) = \mathrm{OPL}(r) - \mathrm{OPL}(r_0) + \frac{\lambda_m}{2\pi}\phi(r), \tag{8}$$

where r_0 is the coordinate of the reference ray (such as the chief ray). It is not necessary to discretise $\phi(r)$ into the effects of individual layers since the coordinates r in the pupil need not be determined with a precision better than the period of the diffracting structure. Chromatic aberrations can be computed when the measurement wavelength λ_m is different to the design wavelength λ.

3.3. Off-Bragg reflections

Equations (7) and (8) can be used to trace rays through the optical system and analyse its wavefront aberrations. These equations do not account for any variation in diffraction efficiency, which drops precipitously for rays outside of the so-called Darwin width of the reflection profile (also referred to as the rocking-curve width), which will occur for rays originating from a source point off the optic axis, for example, as well as for rays incident at the Bragg angle but which have the wrong wavelength. No matter whether a deviation from the Bragg condition is caused by a change in wavelength λ_m or a change in incident ray direction $\hat{\boldsymbol{r}}$, or a combination of both, solving $|\hat{\boldsymbol{r}}'| = 1$ using (7) will generate a non-zero error term ϵ. If the normal $\hat{\boldsymbol{n}}$ is perpendicular to $\boldsymbol{q}$ (which is the case for symmetric Laue diffraction) then the equivalent angular deviation from the Bragg condition can be estimated as

$$\Delta\theta \approx \frac{2\pi\epsilon}{\lambda_m|\boldsymbol{q}|} = \frac{\epsilon d}{\lambda_m}. \tag{9}$$

The diffraction efficiency of a ray as a function of $\Delta\theta$ can be calculated by dynamical diffraction theory [27] or, equivalently, coupled waved theory [30]. Bajt *et al.* [31] and Yan *et al.* [7] give expressions for dynamical diffraction of multilayer structures. In

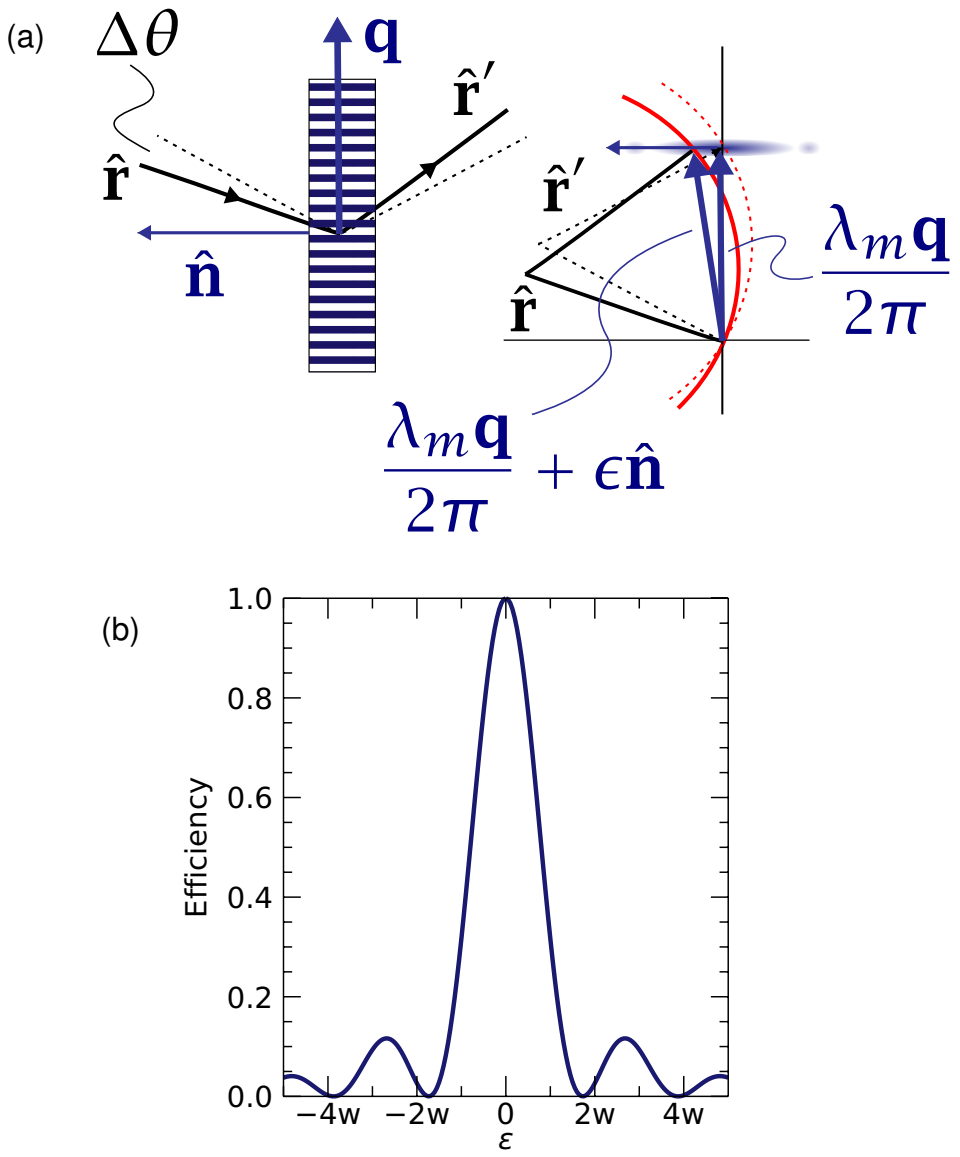

Figure 2. (a) The off-Bragg reflection from a periodic multilayer in Laue geometry shown in real space to to left is found from the reciprocal-space Ewald sphere construction at right, considering that the diffraction peak lies along a truncation rod normal to the surface. (b) Rocking curve of a multilayer reflecting in a Laue geometry with an optimum thickness and neglecting absorption, as a function of the deviation parameter $\epsilon \approx \Delta\theta\, \lambda_m |\boldsymbol{q}|/(2\pi)$ and for a width w_ϵ.

particular, for a thick multilayer grating constructed of equal layer heights of the two materials per period, a thickness of the lens τ, and ignoring absorption, the normalised rocking curve of the symmetric Laue reflection is given by

$$I_L(\eta) = \sin^2\left(\frac{\pi\,\tau}{\Lambda_L}\sqrt{1+\eta^2}\right)\,\frac{1}{1+\eta^2} \tag{10}$$

for a Pendellösung period Λ_L and the normalised deviation parameter η equal to

$$\eta = \frac{\Delta\theta}{w_\theta} = \frac{\Delta\theta\,\pi\,\sin 2\theta}{2|\delta_1 - \delta_2|} \approx \frac{\epsilon\,\pi}{2|\delta_1 - \delta_2|} = \frac{\epsilon}{w_\epsilon} \tag{11}$$

for a Bragg angle θ, and where δ_1 and δ_2 are the real parts of the optical constants of the layer materials at the particular photon energy used. The expression of η in terms of ϵ was obtained from $\sin 2\theta \approx 2\theta \approx \lambda_m/d$. In the following we assume that the MLL is cut at a thickness $\tau = \Lambda_L/2$ to give the maximum diffraction efficiency such that $I_L(0) = 1$. The width of the Laue rocking curve is given by the Darwin width w_θ, at which the efficiency drops to 0.317. The efficiency $I_L(\epsilon/w_\epsilon)$ is plotted in figure 2 (b) and can be included in the ray tracing procedure [20] by multiplying the ray intensity (initially unity) by the diffraction efficiency at each interface. As seen from equations (10) and (11), this calculation does not require any further specification of the d spacing of the multilayer or the wavelength, which are implicitly accounted for in the prescription of $\boldsymbol{q}$, as demonstrated in the next section.

4. Off-axis aberrations of axi-symmetric MLLs

Diffractive optical elements provide extra degrees of freedom for optical design as compared with refractive elements since the phase profile, as determined by the diffracting structure, can be decoupled from the profile of the surface. For example, it can be shown that the Seidel aberration of coma (varying linearly with the field angle) is eliminated for particular imaging conjugates when a zone plate is constructed on a spherical rather than a flat surface [11–13, 32]. When combined with the prescription of zones or layer periods $d(r)$ that result in zero spherical aberration (as given in section 3.1), the appropriately-curved zone plate is thus aplanatic (free of aberrations over a paraxial field of view) and obeys the Abbe sine condition. The required surface of the zone plate is given by the circle of Apollonius, for which the radius R satisfies $1/R = 1/b - 1/a$ for an object distance a and image distance b, and where positive R represents a convex surface as seen from the object plane. For all points on this circle, the ratio of the distances from a point on the circle to either the object or image points is a constant. When $a = \infty$, $R = b = f$, which is the case illustrated in figure 1 (b).

Using the formalism laid out in the previous section we thus analyse the case of an axi-symmetric MLL (as made by depositing materials onto a wire) with conical or paraboloidal layers, imaging a source at $a = \infty$, to determine if there is an advantage to polishing the MLL to a radius R. This serves as an illustrative case to compare with the analysis of imaging with pairs of one-dimensional MLLs and for the examination of MLLs with various imperfections in section 6.

Consider the axi-symmetric MLL shown in figure 3 which is polished to a sphere of radius R (which may differ from the focal length, f). The surface of the MLL is given by the "sag", equal to the distance $z = s(r)$ from the plane at $z = 0$ to the surface, which can be parameterised as

$$\boldsymbol{s}(r, \psi) = \left(r\sin\psi, r\cos\psi, R - \sqrt{R^2 - r^2}\right). \tag{12}$$

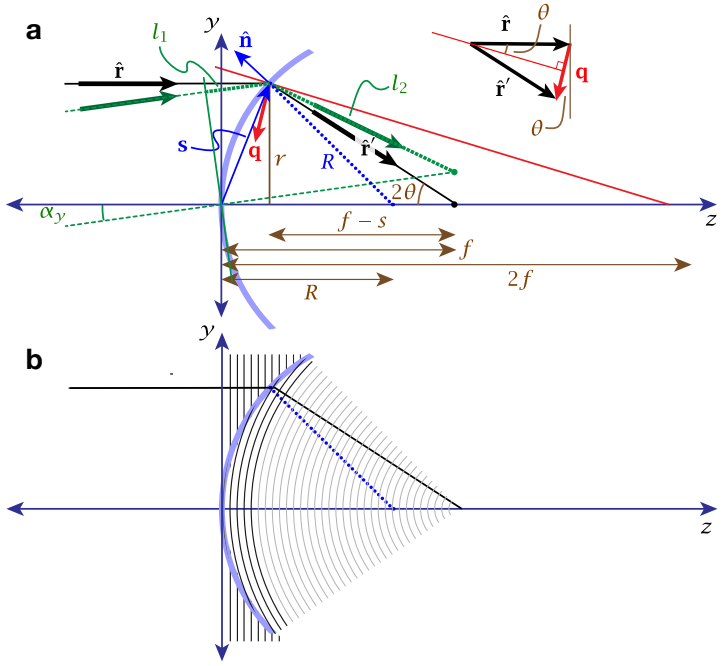

Figure 3. Geometry for ray trace calculations of a single MLL of focal length f. (a) The lens shape is the shell of a sphere or cylinder of radius R, shown in blue, with a surface described by $\boldsymbol{s}(r)$ for the radial coordinate r. Rays are deflected by the diffracting structure described by $\lambda/(2\pi)\boldsymbol{q}(r)$ (in red) and the surface normal $\hat{\boldsymbol{n}}(r)$. This structure fulfils the Bragg condition (see inset) for the on-axis field point at infinity. The path of an incoming ray with direction $\hat{\boldsymbol{r}}$ is shown in black. Paths for rays from a field angle $-\alpha_y$ are shown in green, and the path lengths l_1 and l_2 are indicated for that case by the thick dashed green lines. (b) Deflection of rays is also a consequence of the accumulation of 2π of phase from each layer pair, which themselves match the interference of the on-axis plane wave with a converging spherical wave.

Here we use cylindrical polar coordinates (r, ψ, z), and a positive R corresponds to a centre of curvature towards $+z$. The definition of $\psi = 0$ along the cartesian y axis follows the convention of optical ray tracing. The outward-facing normal to this surface is parallel to the cross product of the gradients of $\boldsymbol{s}$ in the x and y directions, giving a unit normal

$$\hat{\boldsymbol{n}}(r,\psi) = \left(\frac{r}{R}\sin\psi, \frac{r}{R}\cos\psi, -\sqrt{1-\frac{r^2}{R^2}}\right). \tag{13}$$

The MLL is constructed with layers of varying period and tilt designed to perfectly focus incident rays of a particular wavelength λ and parallel to the optic axis (taken to be the z axis) to a point on that axis a distance f from the MLL. Therefore, at a distance r from the optic axis, layers of period $d(r) = \lambda/(2\sin\theta(r))$ are tilted by an angle $\theta(r)$ to reflect rays by $2\theta(r)$ as needed to direct them to the focus. This requires

$$\sin 2\theta(r) = \frac{r}{\sqrt{r^2 + (f-s)^2}} \tag{14}$$

so that the layer periods (not equivalent to the deposited layer thicknesses) are given by

$$d(r) = \frac{\lambda}{2\sin\theta} \approx \frac{\lambda f}{r}\left(1 + \left(\frac{3}{8} - \frac{f}{2R}\right)\frac{r^2}{f^2}\right). \tag{15}$$

More completely, the momentum transfer vector caused by diffraction from the tilted layers is given by

$$\begin{aligned}\frac{\lambda}{2\pi}\,\boldsymbol{q}(r,\psi) &= (-\sin 2\theta(r)\,\sin\psi, -\sin 2\theta(r)\,\cos\psi, \cos 2\theta(r) - 1) \\ &= \left(\frac{-r\sin\psi}{\sqrt{r^2+(f-s)^2}}, \frac{-r\cos\psi}{\sqrt{r^2+(f-s)^2}}, \frac{f-s}{\sqrt{r^2+(f-s)^2}} - 1\right).\end{aligned} \tag{16}$$

This prescription of the layer period is consistent with (4) because the structures described in equations (15) and (16) are located on the surface $z = s(r)$. The phase induced by the diffracting structure that achieves this common focus is given by (3) which can be expressed as

$$\begin{aligned}\frac{\lambda}{2\pi}\,\phi(r) &= s + \sqrt{r^2+(f-s)^2} - f \\ &\approx \frac{r^2}{2f} + \left(\frac{2f}{R} - 1\right)\frac{r^4}{8f^3}.\end{aligned} \tag{17}$$

The functions $\boldsymbol{s}(r,\psi)$, $\hat{\boldsymbol{n}}(r,\psi)$, $\boldsymbol{q}(r,\psi)$, and $\phi(r)$ fully define the structure and optical properties of the MLL. They can be used, with equations (7) and (8), to determine the wavefront aberrations, with the simplifying assumption that the thickness of the MLL in the z direction is negligible.

Now consider an off-axis source point at infinity but located at a field angle $-\alpha_y$ in the direction along $\psi = 0$. Incident rays are all parallel to $\hat{\boldsymbol{r}} = (0, \sin\alpha_y, \cos\alpha_y)$. We must compute the OPL $= l_1 + l_2$ for rays from a plane with a normal $\hat{\boldsymbol{r}}$ (such as the one passing through the origin, defined by $\boldsymbol{x}\cdot\hat{\boldsymbol{r}} = 0$) and the image point at a height $y_i = f\tan\alpha_y$ in the plane a distance $z = f$ from the MLL vertex at the origin. An incident ray intersects the spherical surface of the MLL at the point $\boldsymbol{s}(r,\psi) = (r\sin\psi, r\cos\psi, s)$, and the path-length l_1 from the inclined plane to this point is given by

$$l_1 = \boldsymbol{s}\cdot\hat{\boldsymbol{r}} = r\cos\psi\sin\alpha_y + s\cos\alpha_y. \tag{18}$$

The length l_2 of the ray from $\boldsymbol{s}$ to the image plane depends on its direction $\hat{\boldsymbol{r}}'$ which can be found from (7), utilising equations (16) and (13) and substituting $\sin 2\theta$ for the expression in (14). The incident ray no longer satisfies the Bragg condition, so the error length ϵ must be solved for, which can be done by constraining the magnitude of $\hat{\boldsymbol{r}} + \lambda_m/(2\pi)\,\boldsymbol{q} + \epsilon\hat{\boldsymbol{n}}$ to be unity (for rays of the "measurement" wavelength λ_m). The optical path length of the ray travelling from the MLL to the image plane can be obtained by noting that $l_2\,\hat{\boldsymbol{r}}'\cdot\hat{\boldsymbol{z}} = f - s$.

The analysis can be carried out numerically or using a symbolic mathematics program, which can yield an exact result for the OPD given by

$$\mathrm{OPD}(r) = l_1 + l_2 - \frac{f}{\cos\alpha_y} - \frac{\lambda_m}{2\pi}\phi(r), \tag{19}$$

using the expression for $\phi(r)$ from (17). As noted above, $\phi(r)$ accounts for the number of bi-layers n in the structure from the reference point to r, which give rise to an effective optical path of $n\,\lambda_m$ when measured at a wavelength λ_m. For imaging at the wavelength that the lens was designed, $\lambda_m = \lambda$, the series expansion of the exact expression is found to be

$$\mathrm{OPD}^{(4)}(\rho) = -\frac{3f}{2}\alpha_y^3\rho\cos\psi + f\left(\frac{3}{4} - \frac{f}{2R}\right)(2+\cos 2\psi)\alpha_y^2\rho^2 + f\left(\frac{f}{R} - 1\right)\alpha_y\rho^3\cos\psi, \quad (20)$$

where $\rho = r/f$ is the the normalised pupil coordinate equal to the tangent of the angle of rays converging onto the focus. At the edge of the pupil, $\rho \approx \mathrm{NA}$. Only terms to fourth order in powers of α_y and ρ are retained in this series expression, corresponding to the five Seidel (or primary) aberrations of an axi-symmetric system. In (20) there are three summands. The first varies linearly with the pupil coordinate ρ and indicates a wavefront tilt that grows with the third power of the field angle α_y. This tilt corresponds to a shift of the image point and hence a distortion to the image. The second term consists of astigmatism and field curvature. The dependence on ρ^2 indicates a defocus which is different in orthogonal planes $\psi = 0$ and $\psi = \pi/2$. The last term is coma, an aberration that depends on the third power of the pupil coordinate. The expression of (20) does not contain the Seidel aberration dependent only on ρ^4, which is spherical aberration. This is the only Seidel aberration present for a source point on axis ($\alpha_y = 0$) and since the MLL was designed to have zero aberrations on axis at the design wavelength, this term is also absent in this series approximation. As anticipated above, the case where $R = f$ gives zero coma. It is also interesting to note that the condition $R = (2/3)f$ eliminates astigmatism and field curvature, at the cost of finite coma.

In this analysis we find that changing the condition for off-Bragg reflection modifies the terms in (20), and thus the formulation of (7) does matter. For example, setting $\hat{\boldsymbol{n}}$ to be parallel to the optic axis rather than normal to the spherical surface modifies the distortion and field curvature coefficients.

4.1. Transmission of an axi-symmetric MLL

Since all rays from the on-axis field point exactly match the Bragg condition in the lens, they will be fully transmitted (under the ideal assumptions discussed in section 3.3) and the transmission of the lens will be uniform across the pupil. Rays from off-axis field points will deviate from the Bragg condition with an efficiency $I_L(\epsilon)$ where ϵ is the deviation parameter. An off-axis field angle leads to an angular deviation $\Delta\theta \approx \alpha_y$, so we expect from (9) that $|\epsilon| \approx \lambda\alpha_y/d$. Since the smallest periods d occur at the edge of the lens, the lens will be apodised—it will lose transmission at the outermost regions of the pupil as the field angle is increased from zero. Off-axis field points therefore become vignetted (have lower transmission) [33] with reduced NA and degraded resolution. The expression for ϵ is obtained in the analysis that leads to (20) by solving for $|\hat{\boldsymbol{r}}'| = 1$. The series expansion of this expression to first-order in α_y is given by

$$\epsilon^{(1)}(\rho) = -\alpha_y\rho\cos\psi + \frac{f}{2R}\left(1 - \frac{f}{R}\right)\alpha_y\,\rho^3\cos\psi. \quad (21)$$

That is, the magnitude of the deviation parameter does indeed increase linearly with field angle and also depends linearly on the pupil coordinate in the direction of the field angle, $\rho\cos\psi$. In this direction, lens apodisation occurs when the deviation parameter at the edge of the lens ($\rho = \mathrm{NA}$) exceeds the rocking-curve width, or

$$\alpha_y < \frac{w_\epsilon}{\mathrm{NA}} = \frac{2|\delta_1 - \delta_2|}{\pi\,\mathrm{NA}} = w_\theta. \tag{22}$$

This restriction is independent of the focal length of the lens.

4.2. Chromatic aberrations of axi-symmetric MLLs

The paraxial focal length of a diffractive lens scales inversely with the wavelength, and so such lenses exhibit strong chromatic aberrations dominated by defocus. The design of the layers according to (16) will give zero on-axis aberrations (such as spherical aberration) only for the wavelength at which it was designed. Off-axis aberrations will also be modified with a change in wavelength, since the image of an off-axis source point at infinity will be focused to a plane a distance $f_m = f\,\lambda/\lambda_m$ from the lens with a transverse displacement of $f_m\,\alpha$ from the optic axis instead of $f\,\alpha$. The ray tracing procedure can be carried out using the governing equations of (7) and (8) and solving the path length $l_2 = (f_m - s)/(\hat{\boldsymbol{r}}'\cdot\hat{\boldsymbol{z}})$ to determine the wavefront aberrations encountered when utilising the lens at a different wavelength to its design. In this case it is found that the spherical aberration term is given by

$$\mathrm{OPD}_{\mathrm{SA}}(\rho;\lambda_m) = \frac{3f}{8}\frac{\lambda_m\,\Delta\lambda}{\lambda^2}\left(2 - \frac{2f}{R} + \frac{\Delta\lambda}{\lambda}\right)\rho^4, \tag{23}$$

where $\Delta\lambda = \lambda_m - \lambda$. This expression indicates that in addition to the design wavelength ($\Delta\lambda = 0$), spherical aberration is nulled at the wavelength $\lambda_m = \lambda(2f/R - 1)$. That is, by setting the radius to $R = 2f/(1 + \lambda_m/\lambda)$, the spherical aberration is zero for both λ and λ_m. Of course, images at each of these wavelengths will be located at different planes, so such a design could have utility in scanning transmission or fluorescence microscopy of thick objects at two discrete wavelengths (above and below an absorption edge, for example) with a detector able to discriminate photon energies. Equation (23) also shows that in the limit $\lambda_m \to \lambda$, the optimum radius for minimising the spherical aberration is $R = f$. In this case $\mathrm{OPD}_{\mathrm{SA}}$ varies quadratically with $\Delta\lambda$ instead of linearly.

As with a change in the field angle, rays will no longer obey the Bragg condition as the wavelength is moved from the design. The series expansion of the deviation parameter for the on-axis field point, as determined in the analysis used to derive (23) is given by

$$\epsilon^{(2)}(\rho) = \frac{\lambda_m\,\Delta\lambda}{2\lambda^2}\rho^2. \tag{24}$$

For this on-axis field point, apodisation will therefore occur radially with a tolerance given by

$$\frac{\Delta\lambda}{\lambda} < \frac{2w_\epsilon}{\mathrm{NA}^2} = \frac{4|\delta_1 - \delta_2|}{\pi\,\mathrm{NA}^2}. \tag{25}$$

Both apodisation and spherical aberration may scale approximately linearly with $\Delta\lambda$ (as is the case for a flat lens, for example), but the degree of apodisation increases with the square of the NA whereas spherical aberration grows with the fourth power of NA and linearly with the focal length. Thus for focal lengths shorter than about $0.15\lambda/(\mathrm{NA}^2 w_\epsilon)$, the limitation to wavelength changes will be the reduction of the active pupil diameter. (Here the spherical aberration tolerance from the Marechal condition is $\mathrm{OPD}_{\mathrm{SA}}(\mathrm{NA})/\sqrt{10} < \lambda/14$.)

4.3. Ray tracing an axi-symmetric MLL for 1 nm focusing

As an example, we consider a lens designed to achieve a resolution of about 1 nm at a wavelength $\lambda = 0.075$ nm (17 keV photon energy) and NA = 0.0375. The Rayleigh resolution of this lens for incoherent imaging (such as the case in a scanning transmission microscope) is $0.61\lambda/\mathrm{NA} = 1.22$ nm. The focal length of the lens is chosen to be $f = 1$ mm, and thus the diameter of the lens is 75 µm. The ray-tracing procedure detailed above was used to numerically compute the wavefront aberrations exactly—that is, without approximating to a fourth-order series expansion as for (20). The procedure, as formulated above, applies to the case of field points at infinity, displaced from the optical axis by a field angle α_y as set by the ray direction $\hat{\boldsymbol{r}}$. This situation represents, for example, the formation of a focused beam for a scanning microscope. In this case the field angle also represents the angular misalignment of the optic axis of the lens relative to say a "beam axis" set by the direction of a far-off source. These calculations also correspond to the aberrations expected in full-field imaging at high magnification (where the image plane is far from the lenses and the sample is near to the focal plane). Finite conjugates can be simulated too, with an appropriate re-definition of $\hat{\boldsymbol{r}}$ and l_1.

At the design wavelength the calculated map of the OPD as a function of pupil coordinates for the on-axis field point ($\alpha_y = 0$) is zero to numerical precision, for both the flat MLL ($R = \infty$) and for $R = f$. Thus, the prescription of the layer periods and tilts according to (16) avoid spherical aberration and all other aberrations as desired. The wavefront map for an off-axis field point at $\alpha_y = 1$ mrad for a flat axisymmetric MLL is given in figure 4 (a). This wavefront error, with an RMS value of 0.0062 nm (0.082 wavelengths), is dominated by coma and astigmatism in agreement with (20). Further calculations show that as the field angle increases, coma increases linearly and becomes the dominant term. However, by curving the lens surface such that $R = f$, this term is essentially eliminated, leaving astigmatism as the dominant aberration. For the same field angle of 1 mrad the RMS wavefront for the curved lens is only 0.0001 nm and so the OPD map is not visible on the same scale as for figure 4 (a). Instead, the map is shown for $R = f$ at a field angle of 7.5 mrad in figure 4 (b), after subtracting the best-fit tilt and focus, with an RMS error of 0.0080 nm.

According to the Marechal condition [29], diffraction-limited imaging with a Strehl ratio above 80 % requires an RMS wavefront aberration less than $\lambda/14$, or 0.005 nm in this example. The quarter-wave rule of Rayleigh corresponds to an absolute deviation

of the OPD by 0.019 nm. Thus it is seen that the field angles chosen for the calculations of figure 4 (a) and (b) just slightly exceed the aplanatic region that provides diffraction-limited imaging. The RMS error of both flat and curved lenses is plotted as a function of the field angle in figure 4 (c). It can be seen that by curving the surface of the lens to match the focal length, the radius of the aplanatic field increases from 0.8 mrad to 6.0 mrad. The quadratic dependence of the RMS on field angle for the curved lens indicates this is dominated by the Seidel term for astigmatism in (20). Indeed, after subtracting defocus and tilt, $\mathrm{OPD}^{(4)}(\rho_x, \rho_y) = (f/4)\alpha_y^2(\rho_y^2 - \rho_x^2)$ for $R = f$. The RMS of this aberration over the circular pupil is equal to $f\,\alpha_y^2\,\mathrm{NA}^2/(4\sqrt{6})$. A plot of this curve cannot be distinguished from that shown in figure 4 (c), and the residual RMS aberration after subtracting this term from the numeric computation of OPD is less than 1×10^{-3} nm. Indeed, the contribution of other aberrations besides astigmatism only reach an RMS value equal to $\lambda/14$ at a field angle of 100 mrad. The RMS error is also plotted in figure 4 (c) for the zero-astigmatism condition of $R = (2/3)f$. As mentioned above, coma is still present with $\mathrm{OPD}^{(4)} = (f/2)\alpha_y\,\rho_y^3$, giving rise to the linear dependence of the RMS wavefront error on field angle for lenses with this surface radius.

The aplanatic field of view was calculated here for the angular positions of objects at infinity, but this also corresponds to forming a magnified image in the limit of high magnification. In this case the field of view at the object plane is the field angle multiplied by $f = 1$ mm, or a diameter of 12 µm for the curved lens, which would be increased to 200 µm if the astigmatism were corrected. A well-known approach to do this in lens design is to position the stop at a different plane. For a single refractive surface of radius R, astigmatism can be eliminated by placing the stop a distance $R/2$ from that surface. Unfortunately, this remedy does not work well here since the reduction of astigmatism requires a stop to be placed close to the focal plane. It may be possible, instead, to use a refractive meniscus lens near to the focal plane to change the curvature of the wave-field in the direction of the field displacement and by an amount that increases with that displacement.

As discussed in section 4.1, the field of view of a MLL may be limited not by the field dependence of the aberrations, but rather by the Darwin width of the Laue reflection, proportional to the difference of the optical constants of the materials that make up the layers of the MLL, as given by (22). For SiC and WC layers with densities of 2.47 g cm^{-3} and 14.6 g cm^{-3}, respectively, $|\delta_1 - \delta_2| = 6.7 \times 10^{-6}$ at a wavelength of 0.075 nm, giving a half width of $w_\theta = 2|\delta_1 - \delta_2|/(\pi\,\mathrm{NA}) = 0.11$ mrad for the layers at the boundary of the lens considered here. A plot of the total lens transmission obtained from the numerical analysis of this lens is given in figure 5 as a function of the field angle. Maps of the transmission of the lens pupil are also shown for particular field angles, showing the loss of transmission in the thinner layers first. As seen in the maps, this transmission loss depends only on the projection of the layer period in the direction of the transverse displacement of the field, giving a band of the lens that transmits. The reduction of the aperture leads to a corresponding reduction in resolution in the direction of the

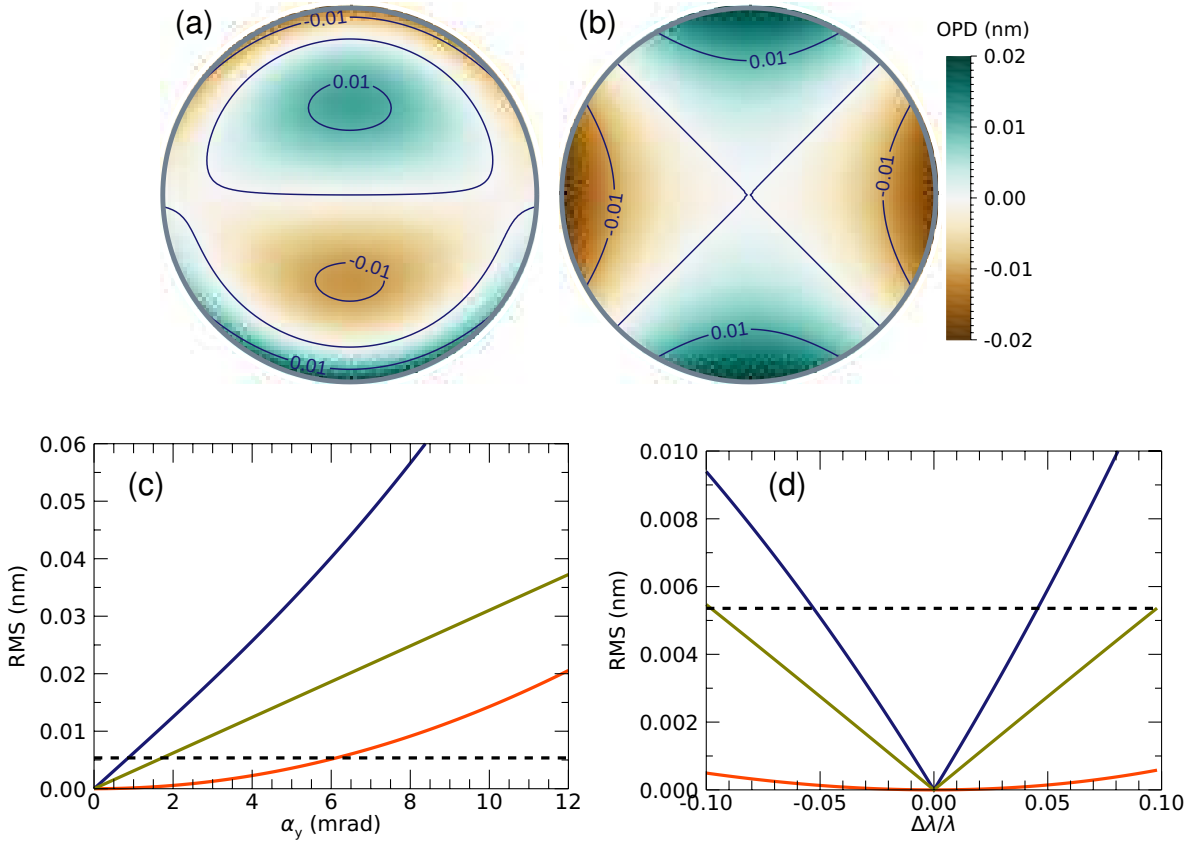

Figure 4. Wavefront errors (excluding defocus) of axisymmetric lenses with NA = 0.0375 and a focal length $f = 1\,\mathrm{mm}$ and (a) a flat surface $R = \infty$ at a field angle $\alpha_y = 1\,\mathrm{mrad}$ and (b) a spherical surface with $R = f$ at a field angle $\alpha_y = 7.5\,\mathrm{mrad}$. (c) Plot of the RMS errors as a function of field angle for $R = \infty$ (blue), $R = (2/3)f$ (olive green) and $R = f$ (red). (d) RMS error as a function of the relative wavelength deviation from the design, where $\Delta\lambda = \lambda_m - \lambda$, and for $R = \infty$ (blue), $R = (2/3)f$ (olive green) and $R = f$ (red). The Marechal condition of $\lambda/14$ is shown by the dashed line for a wavelength of 0.075 nm. The wavefront magnitude scales proportionally with the focal length f.

object or image point (for example, vertical lines will be less resolved than horizontal lines when located at a horizontal position in the field). The lens transmission does not depend noticeably on the radius R.

As seen in section 4.1, the largest field angle that can be tolerated by apodisation due to a loss of diffraction efficiency depends only on the multilayer materials and inversely on numerical aperture, whereas the magnitude of the wavefront aberrations are proportional to the focal length and inversely on powers of the numerical aperture (depending on whether coma or astigmatism dominate). The competition of the effects of the wavefront aberration and apodisation of the pupil on the imaging properties of the lens is illustrated in figure 6 where the combined complex-valued pupil function is shown for various field angles. The square modulus of the Fourier transform of this yields the point spread function (PSF) [28, 29, 34], also shown in the figure. The radius of the aplanatic field for the $f = 1\,\mathrm{mm}$, NA = 0.0375 lens considered here is much larger

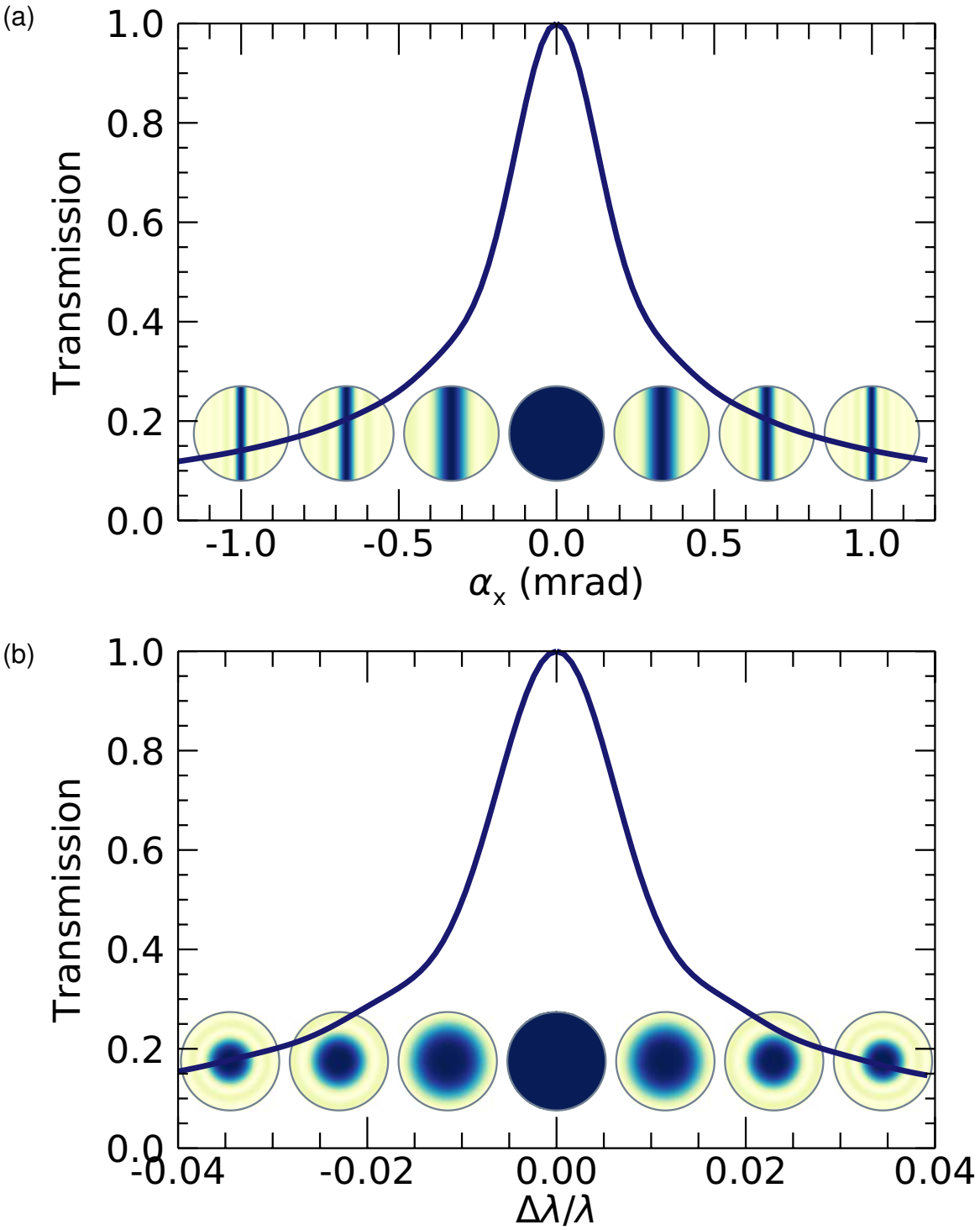

Figure 5. Transmission of an axisymmetric MLL with NA = 0.0375 and a focal length $f = 1\,\mathrm{mm}$ as a function of (a) the field angle, and (b) the relative change in wavelength. In (a) the transmission maps of the lens pupil are shown for field angles $\alpha_x = -1$, -0.6, -0.3, 0, 0.3, 0.6, and 1 mrad, and in (b) for $\Delta\lambda/\lambda = -0.03$, -0.02, -0.01, 0, 0.01, 0.02, and 0.03.

than the limits due to diffraction efficiency, as can be seen in the top row of figure 6. When the field angle exceeds 0.2 mrad (or a image field radius of 0.2 µm) efficiency is lost from two edges of the lens, leading to a broadening of the PSF in the direction of the displacement of the object point. Increasing the focal length of the lens to 10 mm for the same NA (implying a 10 times increase in the lens diameter) leads to a corresponding 10-times increase in the OPD. As seen in the second pair of rows of figure 6, coma causes a degradation of the PSF at lower field angles, before apodisation becomes a problem. Here, the field is limited by the Marechal condition to 0.1 mrad or a field radius of 1 µm. The aberrations can be removed in principle by adopting an aplanatic design by cutting the lens on a spherical surface with a radius $R = f$, giving a performance similar to the 1 mm lens (bottom pair of rows) and an image field radius of about 2 µm (or 2000 resolution elements).

Away from atomic resonances, the optical constants of materials, and hence their difference $|\delta_1 - \delta_2|$, vary with λ^2. For lenses of a given resolution (i.e. made with a minimum d spacing) the NA increases in proportion with λ so that the angular width w_θ is linearly proportional to wavelength. Thus the largest ratio of field of view to resolution is achieved at longest wavelength.

The dominant aberrations induced by a change in wavelength are tilt and defocus due to the change in focal length (which varies inversely with wavelength) and the corresponding change in the paraxial image position. For an on-axis field point the OPD due to defocus is given by $(f/2)(\Delta\lambda/\lambda)\rho^2$ with a RMS value of $(f/4)(\Delta\lambda/\lambda)\mathrm{NA}^2$. Thus, applying the Marechal condition (equivalent to a defocus of less than $(2/7)\lambda/\mathrm{NA}^2$), a relative bandwidth of $2\Delta\lambda/\lambda < (8/14)\lambda/(f\,\mathrm{NA}^2) = 3.0 \times 10^{-5}$ can be tolerated for 1 nm imaging for the lens considered here. A shorter focal length allows a broader bandwidth since this gives fewer periods in the lens.

A MLL manufactured for a particular wavelength might be used at another, for example in spectro-microscopy applications where the sample must be repositioned at the focal distance of $f_m = f\,\lambda/\lambda_m$. The range of wavelengths that can be used depends both on the spherical aberration and the apodisation of the lens caused by the incorrect tilt of the layers for the particular wavelength. The RMS wavefront error is plotted in figure 4 (d) for the on-axis field point as a function of wavelength. Here, the ray-tracing was performed at the paraxial image plane at f_m. As expected from (23), the best compensation is achieved for $R = f$, where the dependence on $\Delta\lambda$ is quadratic. However, as seen from figure 5 (b), and expected from (25), the limitation on using the lens at different wavelengths arises from apodisation, not spherical aberration.

5. Off-axis aberrations of 1D MLLs

Multilayer Laue lenses are typically fabricated by layer deposition onto a flat substrate, to produce a structure that focuses only in one direction, similar to a cylindrical lens. Two crossed cylindrical lenses can focus or form an image in two dimensions, as can two crossed MLLs. The imaging characteristics and off-axis aberrations of such systems differ

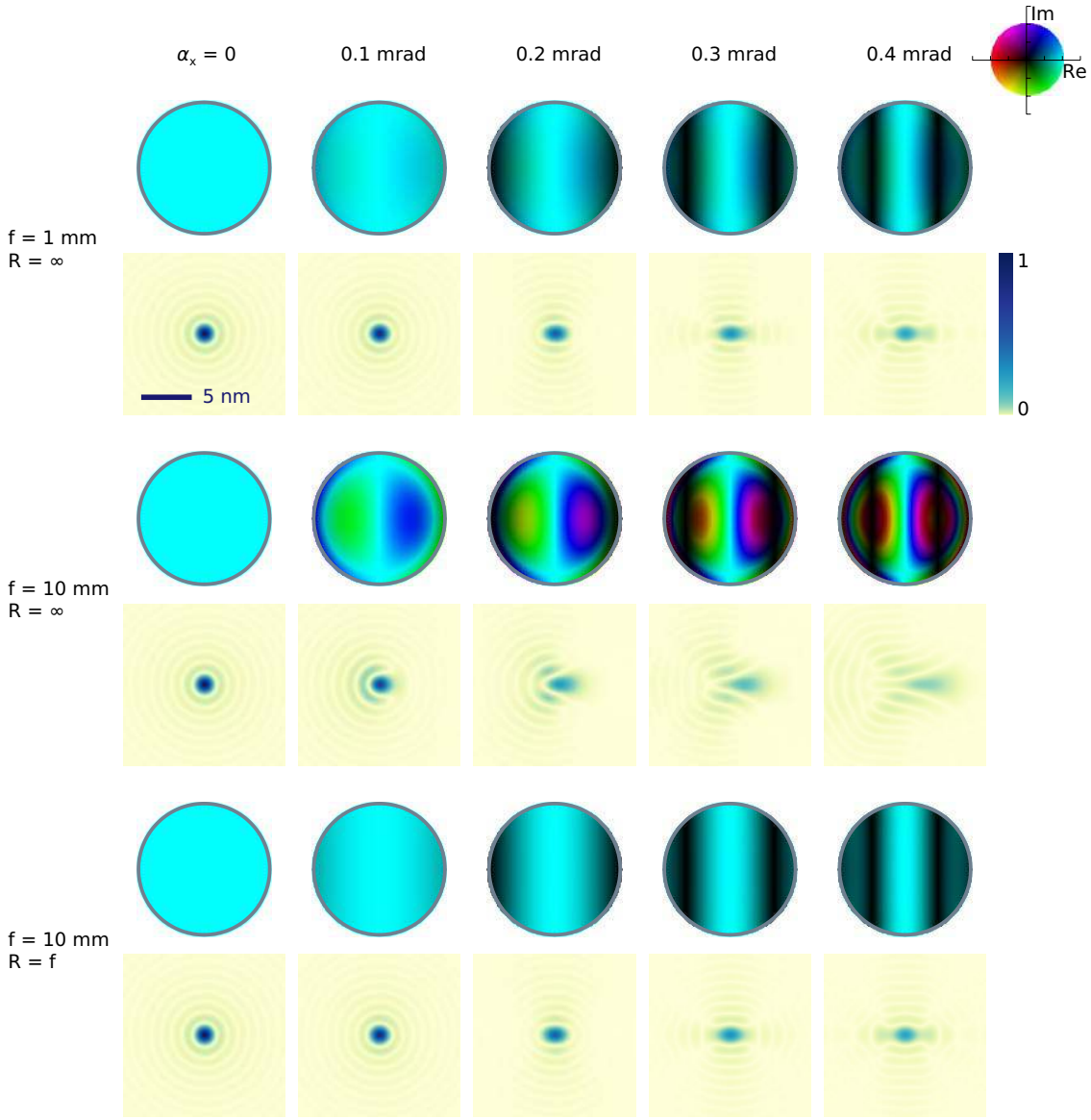

Figure 6. Complex-valued pupil functions of MLLs with NA = 0.0375 for five field angles α_x as indicated, along with their associated point spread functions. Three lens configurations are shown as indicated by the labels to the right. Complex values in the pupil function are visualised by hue (phase) and brightness (amplitude) according to the color-wheel shown at top right.

from axi-symmetric lenses examined above. In particular, crossed MLLs are anamorphic (giving a different magnification in each transverse direction due to the different object and image distances to each lens), the concept of entrance and exit pupils is not well defined, and there are 16 primary aberrations instead of the five Seidel aberrations of an axi-symmetric system [35]. The surface $\boldsymbol{s}_1$, surface normal $\hat{\boldsymbol{n}}_1$, reciprocal vector $\boldsymbol{q}_1$, and accumulated phase ϕ_1 for a 1D MLL focusing in the y direction (and polished to a cylindrical shape of radius R_1 in that same direction) are listed in the left-hand column of table 2 as found by substituting r with y in the expressions for the axi-symmetric

case in section 4, and setting to zero the x components of $\hat{\boldsymbol{n}}$ and $\boldsymbol{q}$.

The case of a single 1D MLL, with layers parallel to the x axis, imaging an off-axis source point at a field angle α_y in the y-z plane is equivalent to the analysis of section 4 for $\psi = 0$. That is, the y-component of the rays obey the expression OPD(r) of (20) with $\psi = 0$:

$$\mathrm{OPD}^{(4)}(\rho_y;\alpha_y) = -\frac{3f_y}{2}\alpha_y^3\rho_y + 3f_y\left(\frac{3}{4} - \frac{f_y}{2R_y}\right)\alpha_y^2\rho_y^2 + f_y\left(\frac{f_y}{R_y} - 1\right)\frac{1}{f_y}\alpha_y\rho_y^3. \tag{26}$$

Thus, aplanatic focusing in one dimension can be achieved by cutting or polishing the MLL to a cylindrical surface with a radius $R_y = f_y$.

The situation is slightly different for field points off the y-z plane. Despite the symmetry of a 1D MLL, we find that a source point at a field angle α_x in the x-z plane is not necessarily focused with zero aberration. This is due to the tilt of the layers in the MLL. An incident ray at a field angle α_x can be obtained by rotating an axial ray about the y axis. However, the $\boldsymbol{q}$ vectors that define the layers in the MLL are not parallel to the y axis, and as such these inclined rays no longer satisfy the Bragg condition. The analysis can be carried out in the same way as in section 4, starting with $\hat{\boldsymbol{r}} = (\sin\alpha_x, \sin\alpha_y, \{1 - \sin^2\alpha_x - \sin^2\alpha_y\}^{1/2})$. The series expansion of the resulting expression for the OPD to fourth order in products of α_x and y yields

$$\mathrm{OPD}^{(4)}(\rho_x,\rho_y) = f_y\,\alpha_x\rho_x - \frac{f_y}{6}\alpha_x^3\rho_x + f_y\left(\frac{3}{4} - \frac{f_y}{2R_y}\right)\alpha_x^2\rho_y^2 + \mathrm{OPD}^{(4)}(\rho_y;\alpha_y), \tag{27}$$

where $\mathrm{OPD}^{(4)}(\rho_y;\alpha_y)$ is given by (26). Equation (27) shows that in this fourth-order approximation the only consequence of tilting the source point out of the y-z plane is distortion and curvature of field. However, as we shall see below, this leads to an aberrated wave-field when two such 1D lenses are crossed orthogonally to image in two dimensions.

5.1. Off-axis aberrations of crossed 1D MLLs

To determine the performance of crossed 1D MLLs we trace rays through an optical system of a 1D MLL focusing in the y direction with a focal length f_1 followed by another focusing in the x direction with a focal length f_2. The distance between the two lenses is set to $f_1 - f_2$ to ensure they both focus to a common point, and for generality the lenses are polished to cylindrical surfaces with radii R_1 and R_2, respectively (see figure 7). The functions describing the geometry and optical properties of the lenses are given in table 2. The calculation of the OPD proceeds as before, but now with a source point located at a position given by the angles α_x and α_y such that incident rays on the first MLL have a direction $\hat{\boldsymbol{r}}_1 = (\sin\alpha_x, \sin\alpha_y, \{1 - \sin^2\alpha_x - \sin^2\alpha_y\}^{1/2})$. These rays are traced a distance l_1 from the plane perpendicular to their direction to the first lens at the position $\boldsymbol{s}_1 = (x_1, y_1, s_1)$, and then deflected to directions $\hat{\boldsymbol{r}}'_1$ as described in sections 4 and 5 (solving for the deviation parameter ϵ_1). A ray intersects the second lens at the point $\boldsymbol{s}_2 = \boldsymbol{s}_1 + l_{12}\,\hat{\boldsymbol{r}}'_1$ after propagating a distance l_{12}. The x component of this expression yields $x_2 = x_1 + l_{12}\,r'_{1,x}$, which can be substituted into the expression

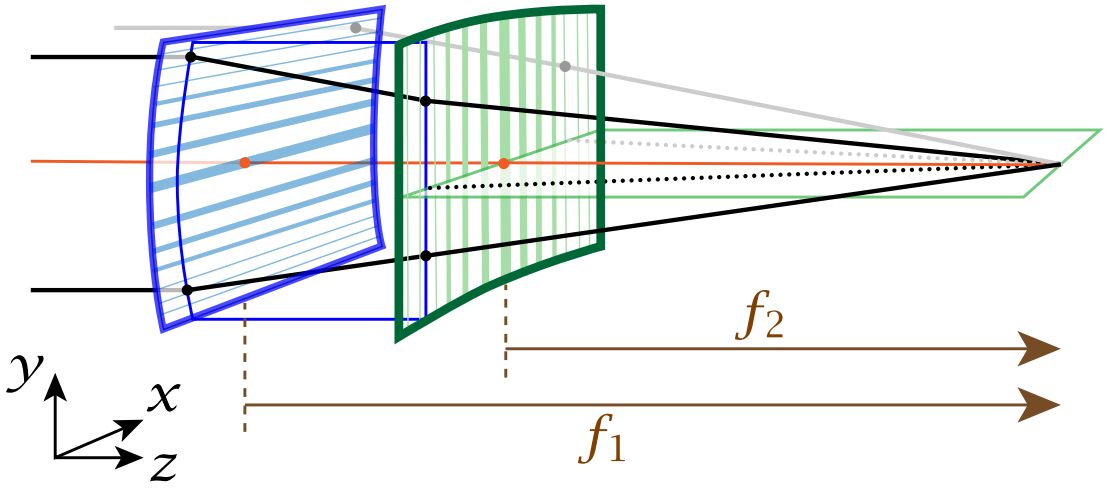

Figure 7. Schematic diagram of two 1D MLLs oriented to focus in orthogonal directions. The first lens focuses in the y direction with a focal length f_1 and the second focuses in the x direction with a focal length f_2, positioned a distance $f_1 - f_2$ from the first. The lenses are also cylindrically curved with radii of curvature R_1 and R_2, respectively.

Table 2. Expressions of the sag s, surface coordinates $\boldsymbol{s}$, surface normal $\hat{\boldsymbol{n}}$, reciprocal vector for diffraction $\boldsymbol{q}$, and phase lag due to the number of periods ϕ, for the two crossed MLLs of focal lengths f_1 and f_2, and radii R_1 and R_2, respectively, separated by a distance $f_1 - f_2$.

First lens (vertex at 0)	Second lens (vertex at $f_1 - f_2$)
$s_1 = R_1 - \sqrt{R_1^2 - y_1^2}$	$s_2 = R_2 - \sqrt{R_2^2 - x_2^2}$
$\boldsymbol{s}_1 = (x_1, y_1, s_1)$	$\boldsymbol{s}_2 = (x_2, y_2, f_1 - f_2 + s_2)$
$\hat{\boldsymbol{n}}_1 = \left(0, \frac{y_1}{R_1}, -\sqrt{1 - \frac{y_1^2}{R_1^2}}\right)$	$\hat{\boldsymbol{n}}_2 = \left(\frac{x_2}{R_2}, 0, -\sqrt{1 - \frac{x_2^2}{R_2^2}}\right)$
$\frac{\lambda}{2\pi}\boldsymbol{q}_1 = \left(0, \frac{-y_1}{\sqrt{y_1^2 + (f_1 - s_1)^2}}, \frac{f_1 - s_1}{\sqrt{y_1^2 + (f_1 - s_1)^2}} - 1\right)$	$\frac{\lambda}{2\pi}\boldsymbol{q}_2 = \left(\frac{-x_2}{\sqrt{x_2^2 + (f_2 - s_2)^2}}, 0, \frac{f_2 - s_2}{\sqrt{x_2^2 + (f_2 - s_2)^2}} - 1\right)$
$\frac{\lambda}{2\pi}\phi_1 = \sqrt{y_1^2 + (f_1 - s_1)^2} - f_1 + s_1$	$\frac{\lambda}{2\pi}\phi_2 = \sqrt{x_2^2 + (f_2 - s_2)^2} - f_2 + s_2$

for s_2 given in table 2 to obtain, from the z component, a quadratic equation that can be solved for l_{12}. The ray at $\boldsymbol{s}_2$ incident at an angle $\hat{\boldsymbol{r}}_2 = \hat{\boldsymbol{r}}_1'$ can then be deflected into the direction $\hat{\boldsymbol{r}}_2'$ that is calculated using (7) and the expressions for $\hat{\boldsymbol{n}}_2$ and $\boldsymbol{q}_2$ in table 2, solving for the off-Bragg deviation parameter ϵ_2 by requiring that $|\hat{\boldsymbol{r}}_2'| = 1$. The distance l_2 from $\boldsymbol{s}_2$ in the second lens to the image plane can be then obtained from $l_2\,\hat{\boldsymbol{r}}_2' \cdot \hat{\boldsymbol{z}} = f_2 - s_2$.

As stated above, two crossed cylindrical lenses do not have a well-defined pupil

(that is, an aperture in a single plane that limits the angular extent of all rays) and therefore this optical system does not have a well-defined chief ray. Nevertheless we can express the OPD as a function of coordinates (x_1, y_1) of the first lens, as the difference between the OPL of a ray that passes through those coordinates and the vertex of that lens, as

$$\mathrm{OPD}(x_1, y_1) = \mathrm{OPL}(x_1, y_1) - \mathrm{OPL}(0, 0) - \frac{\lambda_m}{2\pi}\left[\phi_1(y_1) + \phi_2(x_1 + l_{12}\, r'_{1,x})\right] \tag{28}$$

with $\mathrm{OPL} = l_1 + l_{12} + l_2$ and λ_m is the measurement wavelength. The phase lags ϕ_1 and ϕ_2 are proportional to the number of diffracting periods between the ray of interest and the reference ray, and is thus determined by the coordinate y_1 or x_2 of the ray on the particular lens. Retaining terms to fourth order in pupil and field coordinates, when $\lambda_m = \lambda$ the OPD is evaluated to

$$\begin{aligned}
\mathrm{OPD}^{(4)}(\rho_x, \rho_y) = {} & \frac{3}{4} f_2\, \rho_x^2\, \rho_y^2 \\
& + f_2 \left(\frac{f_2}{R_2} - 1\right) \alpha_x\, \rho_x^3 + f_1 \left(\frac{f_1}{R_1} - 1\right) \alpha_y\, \rho_y^3 \\
& - \frac{3}{2} f_2\, \alpha_y\, \rho_x^2\, \rho_y + \frac{3}{2}(f_1 - 2f_2)\, \alpha_x\, \rho_x\, \rho_y^2 \\
& + \frac{3}{4}\left[4 f_1 \left(\frac{f_2}{R_2} - 1\right) + f_2 \left(7 - \frac{6 f_2}{R_2}\right)\right] \alpha_x^2\, \rho_x^2 + \frac{1}{4} f_1 \left(3 - \frac{2 f_1}{R_1}\right) \alpha_y^2\, \rho_y^2 \\
& + \frac{3}{4} f_2\, \alpha_y^2\, \rho_x^2 + \frac{1}{4}\left[11(f_2 - f_1) + \frac{3 f_1^2}{f_2}\right] \alpha_x^2\, \rho_y^2 \\
& - 3(f_1 - 2f_2)\, \alpha_x\, \alpha_y\, \rho_x\, \rho_y \\
& + \frac{3}{2}(f_1 - 2f_2)\, \alpha_x\, \alpha_y^2\, \rho_x - \frac{1}{2}\left[11(f_2 - f_1) - \frac{3 f_1^2}{f_2}\right] \alpha_x^2\, \alpha_y\, \rho_y \\
& + 3\left(\frac{f_1}{f_2} - 2\right)\left[f_1 \left(\frac{f_2}{R_2} - 1\right) + f_2 \left(\frac{3}{2} - \frac{f_2}{R_2}\right)\right] \alpha_x^3\, \rho_x - \frac{3 f_1}{2}\, \alpha_y^3\, \rho_y
\end{aligned} \tag{29}$$

Here, $\rho_x = x_1/f_2$ and $\rho_y = y_1/f_1$. That is, (ρ_x, ρ_y) are equal to the tangents of the angles of rays converging onto the focus, ignoring deflections of rays in the x direction by the first lens.

There are 14 terms in (29), out of a possible 16 allowed by the symmetry of an anamorphic system [35]. The two absent fourth-order aberrations are the spherical aberration terms of the individual lenses, proportional to ρ_x^4 and ρ_y^4, which are zero by design (as given by the forms of ϕ and $\boldsymbol{q}$). However there is a term in (29) proportional to $\rho_x^2\, \rho_y^2$ which thus varies with the fourth power of the pupil coordinate along the diagonal and is the only aberration for the on-axis field points $\alpha_x = \alpha_y = 0$. It is seen from (29) that the coma terms (proportional to $\alpha_y\, \rho_x^3$ and $\alpha_x\, \rho_y^3$) are zero under the same conditions as for the individual lenses, namely that the curvatures of the lenses are set equal to the focal lengths, $R_1 = f_1$ and $R_2 = f_2$. However, even then, there are some coma-like cross terms (proportional to $\alpha_y\, \rho_x^2\, \rho_y$ and $\alpha_x\, \rho_x\, \rho_y^2$) that are independent of R_1 and R_2. Indeed, the only dependence of the OPD on the radii of curvature occur in terms that are proportional to only x or only y coordinates, and we find through computational ray

tracing that, in general, errors in or modifications to the wavefronts of the individual lenses only affect the wavefront in the corresponding coordinate of the system wavefront. Thus, a radius of curvature of the lenses equal to their focal lengths does reduce coma, and does minimise off-axis aberrations, but it does not produce an aplanatic system as is achievable for an axi-symmetric lens. The remaining terms of (29) are either quadratic in the pupil coordinates, representing curvature of field and astigmatism, or linear in pupil coordinates, describing image distortion. The field-dependent 45° astigmatism (or more correctly, oblique astigmatism), proportional to $\rho_x\,\rho_y$, is zero for $f_2 = f_1/2$, as are some of the other terms. When $f_1 = f_2 = R_1 = R_2$ the expression for OPD is invariant in swapping the x and y coordinates ($\rho_x \leftrightarrow \rho_y$ and $\alpha_x \leftrightarrow \alpha_y$) as expected.

The minimum aberration occurs for a field point on axis, and unlike the case of the individual lenses this aberration is non-zero, with OPD $= (3/4) f_2\,\rho_x^2\,\rho_y^2$. This non-zero aberration exists even though each individual lens focuses an incident collimated beam without aberration. It can be termed "oblique spherical aberration" since it varies with the fourth order of the pupil radial coordinate along the diagonal ($\psi = 45°$ for a square pupil), and is zero in the x and y directions. For on-axis cylindrical lenses where ρ_x and ρ_y range from $-$NA to $+$NA, the RMS wavefront error is evaluated to $(3/20) f_2\,\mathrm{NA}^4$. This can be compensated slightly by introducing defocus proportional to $\rho_x^2 + \rho_y^2$, reducing the RMS wavefront error to a minimum of $\sqrt{2/7}(3/20) f_2\,\mathrm{NA}^4 = 0.11 f_2\,\mathrm{NA}^4$. This error is significant for high-NA lenses for imaging at 1 nm resolution. For example, for NA $= 0.0375$, $\lambda = 0.075\,\mathrm{nm}$, and $f_2 = 1\,\mathrm{mm}$, the RMS error is equal to $0.16\,\mathrm{nm} = 2.1$ waves, excluding tilt, defocus, and astigmatism. The Marechal condition at this wavelength (i.e an RMS wavefront less than $\lambda/14 = 0.005\,\mathrm{nm}$) can be satisfied for lenses with a 1 mm focal length only for NA < 0.016, or a resolution of 2.3 nm. Alternatively, a resolution of 1 nm at this wavelength requires a focal length $f < 34\,\mu\mathrm{m}$. Such a lens would have a very small aperture, so a more practical approach would be to compensate the on-axis aberration with an appropriately shaped refractive phase plate [36], akin to a Schmidt corrector plate [37].

The $\rho_x^2\,\rho_y^2$ error is not dependent on the curvatures of the surfaces of the individual lenses, nor the distance between them, and is independent of the field angle. The origin of this error can be traced to the curvature of field of the second MLL (here focusing in the x direction) due to rays incident out of the x–z plane. This is the situation addressed by (27) (but with the x and y directions reversed). That is, consider rays from the on-axis field point with $\hat{\boldsymbol{r}}_1 = (0, 0, 1)$ intersecting the first MLL at a particular height y_1 and a range of values x_1. These will be all be deflected in the y direction by the same angle, $\alpha_y \approx y_1/f_1$, and will impinge on the second lens with this angle, leading to a defocus term that according to (27) is proportional to $\alpha_y^2\,x_1^2$ and thus to $x_1^2\,y_1^2$. One may expect that this could be addressed by polishing the surface of the second lens to a cylinder of radius f_2 that curves in the y direction so that the rays deflected by the first lens always impinge normal to the surface (and hence seem to always be on axis). Failing that, setting $R_2 = (2/3) f_2$ may eliminate the curvature of field as suggested by (27). The ray-trace analysis shows, however, that the on-axis aberration remains unchanged

for any choice of curvature, as given by the term in (29). The wavefront is dependent upon the tilts of the diffracting layers in the MLL, which follow the cylindrical symmetry dictated by their deposition onto flat substrates. The normals of the layers of the second lens are in the x-z plane as described by $\boldsymbol{q}_2$ in table 2.

The transmission of the lens system is also affected by the violation of the Bragg condition in the second lens. For the on-axis field point, the analysis leading to (29) gives the solution of the deviation parameter of the first lens as $\epsilon_1(\rho_x, \rho_y) = 0$, showing that the Bragg condition is satisfied across the entire pupil of the first lens, but in the second lens

$$\epsilon_2^{(4)}(\rho_x, \rho_y) = \rho_x^2 \rho_y^2 / 4. \tag{30}$$

This equation suggests that the loss of transmission of the lens starts to occur at the corners of the pupil ($\rho_x = \rho_y = \mathrm{NA}$), even for the on-axis field point, when $\mathrm{NA}^4 > 4w_\epsilon$, independent of focal length. For the SiC/WC multilayer system considered above for a wavelength of 0.075 nm where $|\delta_1 - \delta_2| = 6.7 \times 10^{-4}$, (30) sets a limit of the NA of crossed 1D lenses to 0.064, corresponding in this case to a resolution of 0.59 nm.

Equation (30) confirms that the on-axis aberration stems from the fact that the convergent beam incident on the second lens does not mirror the reference wavefront that conceptually would produce the design of the second MLL as a computer-generated hologram. An elimination of the on-axis aberration (and the apodisation) would thus require that the layers of the second lens are fabricated to conform to the cylindrical symmetry introduced by the first lens and the desired spherical convergent beam created by the second. The use of a phase plate, as suggested above, would address the aberration but not the lens transmission.

5.2. Relative alignment of the two lenses

From the cylindrical symmetries of the two lenses, any transverse displacement of one lens relative to the other either leaves the system invariant or simply shifts the optic axis, defined by the y coordinate of the first lens and the x coordinate of the second lens (see figure 7). A tilt of one lens about either the x or y axes will cause an aberration of similar magnitude as that from a field angle α_y or α_x. However, in that case there no longer exists an axis of symmetry of the system, and instead one can consider the coordinate system to be fixed to one of the lenses, such that a tilt of that lens is equivalent to an opposite change in the field angle. Alignment tolerances are investigated in section 5.5 for lenses with 1 nm resolution.

As known from the analysis of crossed cylindrical lenses, an error in the orthogonality of the two lenses, caused by a rotation of one relative to the other about the z axis, leads to oblique astigmatism with a wavefront error proportional to $\rho_x \rho_y$ [9]. This can be seen in the simplifying approximation of the system wavefront as the sum of the phase contributions of each lens, scaled to to the coordinates of the second lens, given by $\lambda/(2\pi)\,\phi_1 = -y^2/(2f_2)$ and $\lambda/(2\pi)\,\phi_2 = -x^2/(2f_2)$. The combined wavefront of $-f_2(\rho_y^2 + \rho_x^2)/2$, represents (in the paraxial approximation) a spherical

wave converging onto the focus at f_2. However, if the second lens is rotated about the optic axis by an angle χ_z then the second lens produces a phase proportional to $-f_2(\rho_x \cos\chi_z + \rho_y \sin\chi_z)^2$. For small χ_z the wavefront error found by subtracting the converging spherical wave is then equal to $f_2\,\chi_z\,\rho_x\,\rho_y$. This is oblique (45°) astigmatism, and this contribution is constant across the field. This term is orthogonal to the 0°-90° astigmatism and to defocus, and gives an RMS error of $f_2\,\chi_z\,\mathrm{NA}^2/3$. Given a tolerable degree of astigmatism of half a wave, the requirement on the alignment of the two lenses is then $\chi_z < 3\lambda/(2f_2\,\mathrm{NA}^2)$. For the example above of $\lambda = 0.075\,\mathrm{nm}$, $f_2 = 1\,\mathrm{mm}$, and $\mathrm{NA} = 0.0375$ we find a requirement of $\chi_z < 80\,\mu\mathrm{rad}$. This tolerance can in some cases be relaxed by finding the field location with an oblique astigmatism that cancels this term due to the non-orthogonality. As seen in (29), the coefficient of the field-dependent oblique astigmatism is $-3(f_1 - 2f_2)\,\alpha_x\,\alpha_y$. However, choosing the appropriate α_x and α_y to zero the oblique astigmatism will introduce other off-axis aberrations.

5.3. Chromatic aberrations of crossed MLLs

Due to the anamorphism of crossed MLLs, and the fact that focal length scales inversely with λ_m, a change in wavelength causes a different amount of defocus in each focused direction. That is, besides defocus, crossed MLLs exhibit a chromatic astigmatism that is proportional to the difference in focal lengths $f_1 - f_2$. The magnitude of off-axis aberrations (including distortion) will also depend on the field direction. For the on-axis field point, the chromatic defocus and astigmatism can be compensated by repositioning the lenses so that their distances to the image plane are $f_1\,\lambda/\lambda_m$ and $f_2\,\lambda/\lambda_m$ (respectively for the first and second lenses). As in section 4.2, the ray tracing procedure can be carried out for the repositioned lenses for $\lambda \neq \lambda_m$, in which case the on-axis wavefront aberration is evaluated to

$$\begin{aligned}\mathrm{OPD}_{\mathrm{SA}}(\rho;\lambda_m) = {} & \frac{3}{4} f_2 \frac{\lambda_m^3}{\lambda^3}\,\rho_x^2\,\rho_y^2 + \frac{3f_1}{8}\frac{\lambda_m\,\Delta\lambda}{\lambda^2}\left(2 - \frac{2f_1}{R_1} + \frac{\Delta\lambda}{\lambda}\right)\rho_y^4 \\ & + \frac{3f_2}{8}\frac{\lambda_m\,\Delta\lambda}{\lambda^2}\left(2 - \frac{2f_2}{R_2} + \frac{\Delta\lambda}{\lambda}\right)\rho_x^4. \end{aligned} \tag{31}$$

The coefficients of the ρ_y^4 and ρ_x^4 terms of (31) are equivalent to the spherical aberration term for the axisymmetric lens of (23). These terms represent a distorted spherical aberration, which can be zeroed independently in each direction, for a given λ_m, with the appropriate radius of curvature R_1 and R_2. As for the axisymmetric lens, setting $R_1 = f_1$ and $R_2 = f_2$ gives a quadratic dependence of the spherical aberration on the wavelength deviation $\Delta\lambda$ and therefore the lowest chromatic aberration for positive and negative wavelength deviations from the design wavelength. However, even though these terms can be minimised, the oblique spherical aberration (proportional to $\rho_x^2\,\rho_y^2$) scales with $(\lambda_m/\lambda)^3 = (1 + \Delta\lambda/\lambda)^3$ and therefore dominates.

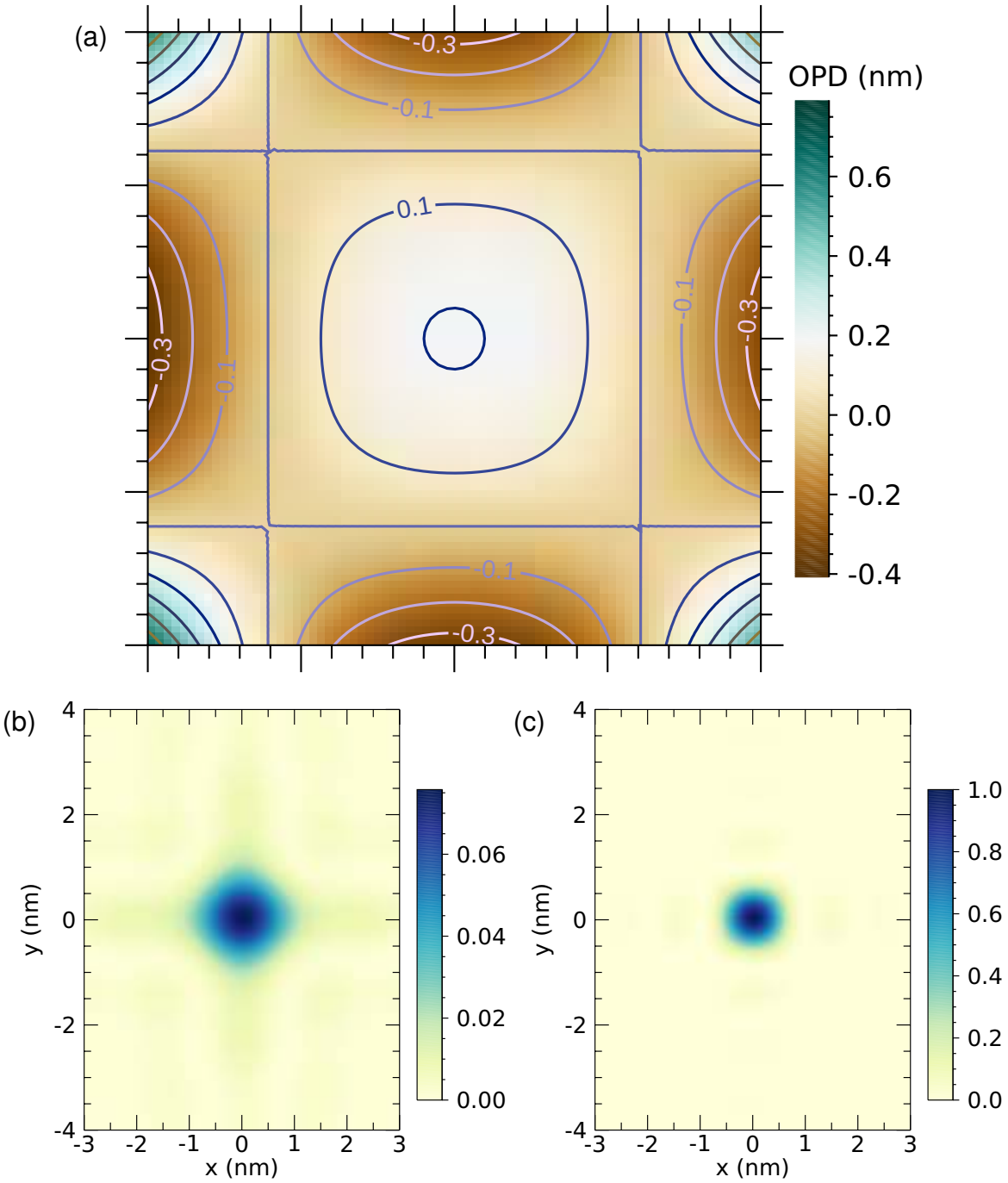

Figure 8. (a) Map of the wavefront aberration for the on-axis field point for a system of crossed flat 1D MLLs of focal lengths of 1.25 mm and 1 mm, both with NA = 0.0375. The best-fit defocus has been subtracted. (b) The point spread function intensity computed from the wavefront aberration for the on-axis field and a wavelength of 0.075 nm, and (c) the point spread function at the same wavelength and NA but zero wavefront aberration.

5.4. Ray tracing of crossed MLLs for 1 nm focusing

As an example, we consider the above-mentioned lens system with a resolution of 1 nm at a wavelength $\lambda = 0.075$ nm (17 keV photon energy) with a square exit pupil of

NA = 0.0375 in the x and y directions, (and NA = 0.053 along the diagonal). Here we define the resolution for a square-pupil optic to be $0.5\lambda/\mathrm{NA}$ in the x and y directions. The focal lengths of the lenses are taken to be $f_1 = 1.25\,\mathrm{mm}$ and $f_2 = 1\,\mathrm{mm}$, and thus the heights of the lenses are 93 µm and 75 µm, respectively. The ray-tracing procedure detailed above was used to numerically compute the wavefront aberrations exactly—that is, without approximating to a fourth-order series expansion as for (29). The particular procedure applies to the case of field points at infinity, displaced from the optical axis by field angles α_x and α_y as set by the ray direction $\hat{\boldsymbol{r}}_1$. This situation represents, for example, the formation of a focused beam for a scanning microscope. In this case the field angles also represent the tilt of the optic axis of the lenses relative to say a "beam axis" set by the direction of a far-off source. The calculations also correspond to the aberrations expected in full-field imaging at high magnification (where the image plane is far from the lenses and the sample is near to the focal plane).

The aberrations are computed in terms of the points of intersection of rays on the two lenses. A map of the OPD as a function of the coordinates of the second lens is shown in figure 8 (a), for flat lenses ($R_1 = R_2 = \infty$). The extent of the plot is limited to the same numerical aperture of 0.0375 in the two orthogonal directions. The best-fit defocus has been subtracted and this map represents the phase error of the exit wave converging onto the plane of best focus. This map is dominated by the fourth-order term $\rho_x^2\,\rho_y^2$, and the residual after subtracting that term from the calculated OPD is proportional to higher order terms with the same symmetry as displayed in figure 8 (a). The RMS wavefront error of the OPD shown in figure 8 (a) is 0.134 nm, compared with the contribution of the fourth-order term $0.08 f_2\,\mathrm{NA}^4 = 0.158\,\mathrm{nm}$. As previously, the point spread function (PSF) can be computed from a Fourier transform of the complex-valued pupil function of the lens system, constructed from the OPD and lens transmission. The PSF for the on-axis field point of the lens system is shown in figure 8 (b) for a wavelength of 0.075 nm, compared with the PSF for a perfect system of the same NA and wavelength in figure 8 (c). In addition to the increased width of the PSF with a full-width at half maximum of 1.64 nm, compared with 0.85 nm for the perfect system, the Strehl ratio of the PSF is 0.076.

The calculated OPD for the on-axis field point far exceeds both the Marechal condition of the RMS error being less than $\lambda/14$ or the Rayleigh condition of an absolute deviation of the OPD by more than $\lambda/4$. Further computations show that the OPD at field angles less than about 1 mrad appear similar to the on-axis aberration map, so we would expect to achieve aplanatic imaging over a field of view of about this extent by compensating the wavefront equally at all field points. Such a compensation could be achieved by locating a phase plate close to either of the lenses.

The aberrations of such a phase-compensated system were simulated simply by subtracting the OPD computed for $\alpha_x = \alpha_y = 0$ from wavefront maps at other field angles. This should be a valid assumption when the phase plate is close enough to the second lens that its correction is the same for all field angles. The wavefront map for the field located at $\alpha_x = 1.25\,\mathrm{mrad}$ and $\alpha_y = 1\,\mathrm{mrad}$ is given in figure 9 (a). The RMS error

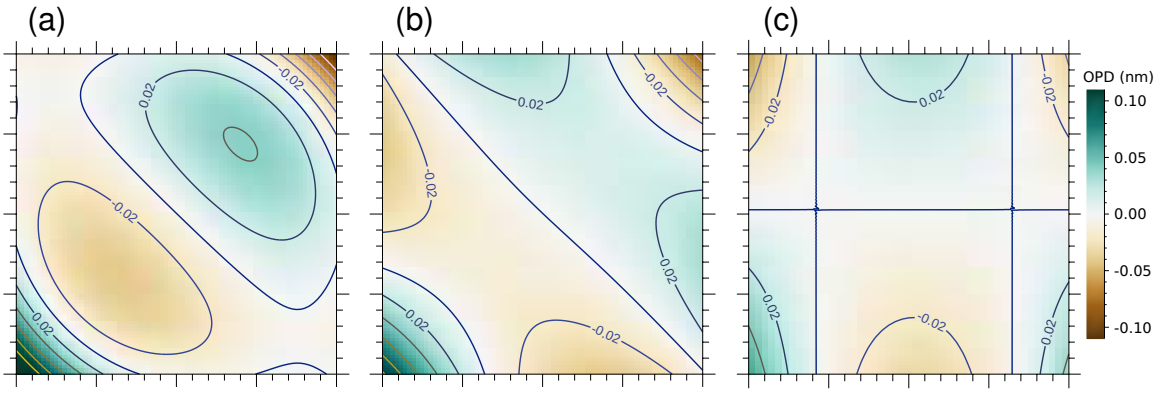

Figure 9. Wavefront maps of systems of crossed 1D MLLs that are phase-compensated for the on-axis field point, calculated over the square pupil (set to be at the second lens) for the field point located at angles $\alpha_x = 1.25\,\text{mrad}$ and $\alpha_y = 1\,\text{mrad}$, for (a) flat MLLs, (b) MLLs with radii of curvature equal to the focal lengths ($R_1 = f_1$ and $R_2 = f_2$), and (c) as for (b) but with $f_1 = 2f_2$. In all cases $f_2 = 1\,\text{mm}$. In (a) and (b) $f_1 = 1.25\,\text{mm}$, while in (c) $f_2 = 2\,\text{mm}$. In all cases the best-fit defocus and 0°-90° astigmatism were subtracted.

is 0.024 nm, which is certainly an improvement over the non-compensated lens system, but still does not meet the Marechal condition. It is apparent from this figure that the wavefront is dominated by coma oriented along the same direction as the field point ($\psi = 45°$, accounting for the anamorphism). That is, the wavefront is proportional to $\rho_x^3 + \rho_y^3$. These are the terms in the second line of (29), which can be eliminated by setting the radii of curvature of the lenses equal to the focal lengths. Figure 9 (b) shows the calculated wavefront for that case. The wavefront aberration is reduced slightly (especially along the $\rho_y = -\rho_x$ diagonal), and the RMS error is also slightly improved with a value of 0.019 nm. The aberration is still dominated by coma, now given by the terms on the third line of (29). Equation (29) suggests one more optimisation to reduce the wavefront aberration, which is to set the focal length of the second lens to half that of the first, $f_2 = f_1/2$, to eliminate one of the remaining two coma-like terms. With this, and cylindrical curvatures of the two lenses equal to the focal lengths, we find the lowest RMS error of 0.014 nm and the map of the wavefront given by figure 9 (c). Here there is a remaining coma-like term that only depends on the position of the field in the y direction, which is the focusing direction of the first lens.

Given a linear dependence on the field angle for coma, achieving the Marechal condition of 0.005 nm RMS aberration error therefore requires reducing the magnitude of the field angle to about a quarter to a third of the value simulated in figure 9 and thus we expect the aplanatic region to have a radius of about 0.3 mrad. Plots of the RMS error as a function of the field position (α_x, α_y) are given in figure 10 for the same lens configurations as for figure 9, with the additional case of flat lenses with $f_1 = 2f_2$. The aplanatic area is indicated by a dashed line, which gives the contour for an RMS of $\lambda/14 \approx 0.005\,\text{nm}$. Comparing Figs. 10 (a) and (b), it is seen that setting the radii of the

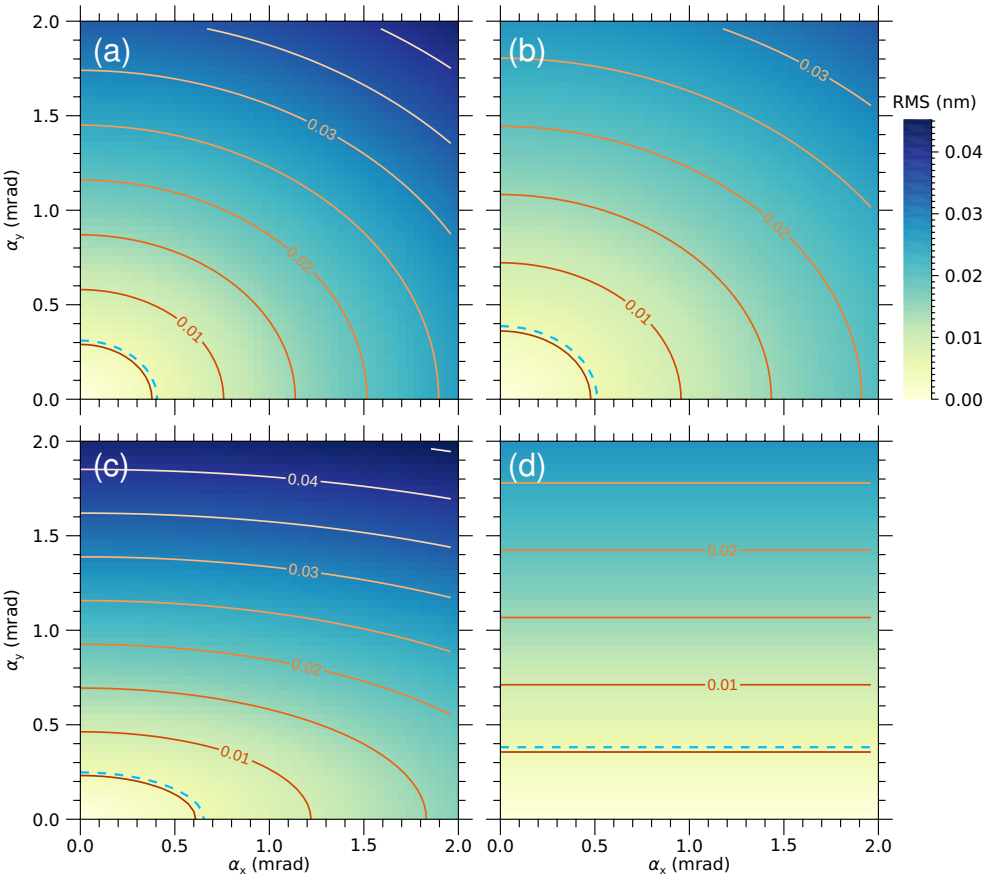

Figure 10. Maps of the RMS wavefront aberration as a function of the field angles α_x and α_y for crossed MLLs with NA = 0.0375, a phase plate set to conjugate the aberration of the on-axis field point, and the focal length of the second lens $f_2 = 1\,\mathrm{mm}$. (a) $f_1 = 1.25\,\mathrm{mm}$, $R_1 = R_2 = \infty$; (b) $f_1 = 1.25\,\mathrm{mm}$, $R_1 = f_1$, and $R_2 = f_2$; (c) $f_1 = 2f_2$, $R_1 = R_2 = \infty$; and (d) $f_1 = 2f_2 = 2\,\mathrm{mm}$, $R_1 = f_1$, and $R_2 = f_2$. The blue dashed lines indicate the Marechal condition of $\lambda/14$ for $\lambda = 0.075\,\mathrm{nm}$. These lines enclose the isoplanatic areas of the lens systems.

lenses to the focal lengths only provides a slight enlargement of the aplanatic area over the case of flat lenses. The RMS error increases linearly with the magnitude of the field angle in these cases, indicating coma in accordance with the terms of (29). The largest aplanatic field (and hence the largest tolerance for misalignment of lenses) is achieved by setting the focal length of the second lens to half that of the first, as in figure 10 (c) and additionally curving each lens to a radius equal to the focal length as depicted in Fig 10 (d).

Plots of the RMS wavefront error as a function of the relative wavelength deviation $\Delta\lambda/\lambda = \lambda_m/\lambda - 1$ for the on-axis field point are given in figure 11, for the cases of curved lenses ($R_1 = f_1$ and $R_2 = f_2$) and flat lenses ($R_1 = \infty$ and $R_2 = \infty$), as computed by ray tracing. It is assumed in these calculations that both lenses are refocused for

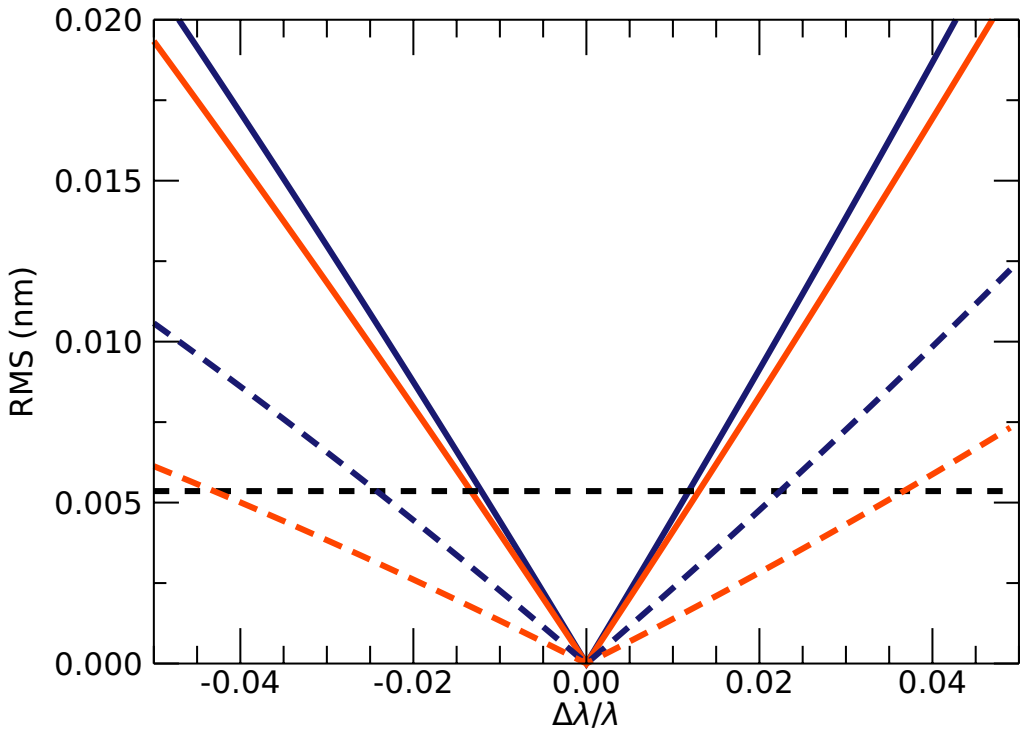

Figure 11. RMS wavefront aberration (excluding defocus and astigmatism) of crossed MLLs of NA = 0.0375, $f_1 = 1.25\,\mathrm{mm}$ and $f_2 = 1\,\mathrm{mm}$ as a function of the relative deviation of the wavelength from the design for curved lenses ($R_1 = f_1$ and $R_2 = f_2$) (orange) and flat lenses ($R_1 = \infty$ and $R_2 = \infty$) (blue). The solid lines assume a corrector with a phase profile that is independent of wavelength and the dashed lines are for a phase corrector made of carbon. The Marechal condition of $\lambda/14$ is indicated by the black dashed line.

each wavelength change. As compared with the aberrations for the axisymmetric lens, plotted in figure 4 (d), the RMS wavefront error is larger for the crossed lenses. It is found that the dominant aberration is proportional to $\rho_x^2\,\rho_y^2$, as expected from (31). The calculations of the RMS errors given by the solid lines in figure 11 furthermore assume that this error is corrected at $\Delta\lambda = 0$, for example by a phase plate, but that the correction is independent of wavelength. However, the refractive index decrement δ of a phase plate constructed from a material of low atomic number such as carbon (diamond) varies as λ^2 at wavelengths comparable to the design wavelength of 0.075 nm. In this case, given that the phase of the corrector is much less than unity, the correction scales as $(\lambda_m/\lambda)^2$. This somewhat compensates for the $(\lambda_m/\lambda)^3$ dependence of the $\rho_x^2\,\rho_y^2$ aberration of the crossed lenses, giving lower RMS errors plotted as dashed lines in figure 11.

As with the case for the axisymmetric lens, the Darwin width of the Bragg reflections of these particular crossed lenses limits the field angles more stringently than the wavefront aberrations. A map of the total transmission of the lens pair is

given in figure 12 (a) as a function of field angle, for the same multilayer properties as in the calculations of figure 5: $|\delta_1 - \delta_2| = 6.7 \times 10^{-6}$. For $\lambda = 0.075\,\mathrm{nm}$ the half width $w_\theta = 0.11\,\mathrm{mrad}$, as for the axisymmetric lens. The transmission is found to be independent of the radii of the lenses, as expected from (30). Likewise, the apodisation caused by detuning the wavelength has a similar behaviour to that found for the axisymmetric lens. As seen in figure 12 (b), a deviation of the wavelength causes the effective numerical aperture of the lens to decrease, and a transmission of at least 0.5 requires $\Delta\lambda/\lambda < 0.9\,\%$.

5.5. Relative alignment of crossed MLLs for 1 nm focusing

The two lenses must be oriented with respect to each other by angles that are comparable to the allowable field angles. The tolerance can be explored by considering one lens to be fixed (which sets the coordinate system) and setting the tilt of the other lens and the field coordinates as free parameters. Ignoring the orthogonality of the lenses (which was discussed in section 5.2) this four-dimensional space is illustrated in figure 13. Here ray tracing calculations are presented for two flat lenses ($R_1 = R_2 = \infty$). The second lens was held fixed and the first tilted by χ_x about an axis passing through its vertex parallel to the x axis or by an angle χ_y about the y axis. The tilt by χ_x is given in the left-hand column of the figure. This tips the lens in the direction that it focuses (refer to figure 7) and it is seen that rays incident on the lens at that tilt angle are efficiently transmitted through it and the second lens, as indicated by the false-colour maps of the transmission as a function of field angle. That the region of high transmission tracks the tilt angle of the lens shows that the transmission of the second lens (which focuses in the x direction) is not sensitive to misalignment in the y direction. The contours in the maps of figure 13 show the RMS wavefront aberration. For the tilts of χ_x (the left column) the aplanatic area shrinks and only tracks the tilt at about a third of the rate of the lens tilt. Thus, the region of the field with low aberrations moves out of the region of high transmission and the tolerable magnitude of the lens tilt χ_x (where the system gives high transmission and low aberrations) is about 0.2 mrad.

The situation is somewhat more relaxed for tilts of the first lens by χ_y about the y axis, as displayed in the right-hand column of figure 13. Just as the χ_x tilt had little effect on the transmission of the second lens, the tilt of χ_y has little effect on the transmission of the first lens. Therefore, the map of the transmission of the lens system remains unchanged. However, the aplanatic region of the field tracks with about half the rate of the lens tilt and does not diminish in area as rapidly as for χ_x tilts. The tolerable magnitude of the χ_y tilt is about 0.4 mrad. This tilt of the first lens by χ_y is equivalent to a rotation by $-\chi_y$ of the second lens about the axis that passes through its vertex parallel to y, combined with a rotation of the field angle. Although the dependence of the aberrations on field angle differs for different values of R_1, R_2, and the ratio of focal lengths, it is found that the tolerances of the lens misalignment remain approximately the same for the various cases that were investigated in figure 10.

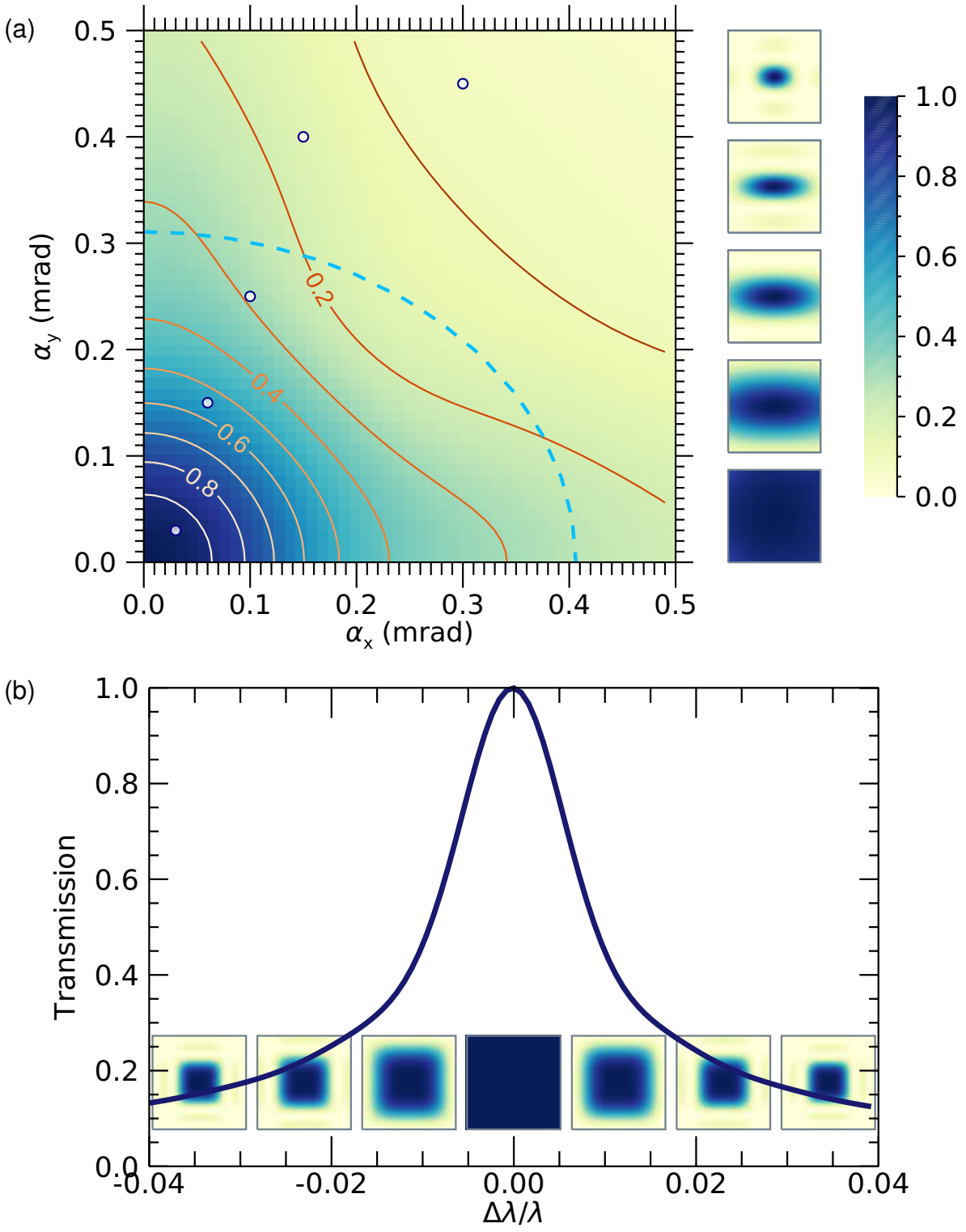

Figure 12. Transmission of crossed MLLs with NA = 0.0375 and focal lengths $f_1 = 1.25\,\mathrm{mm}$ and $f_2 = 1\,\mathrm{mm}$ as function of (a) the field position and (b) the relative change in wavelength. Transmission maps of the square lens-pair pupil are shown in (a) for the positions indicated by the white circles. The Marechal condition for flat lenses and a wavelength of 0.075 nm is indicated by the dashed sky-blue line in (a).

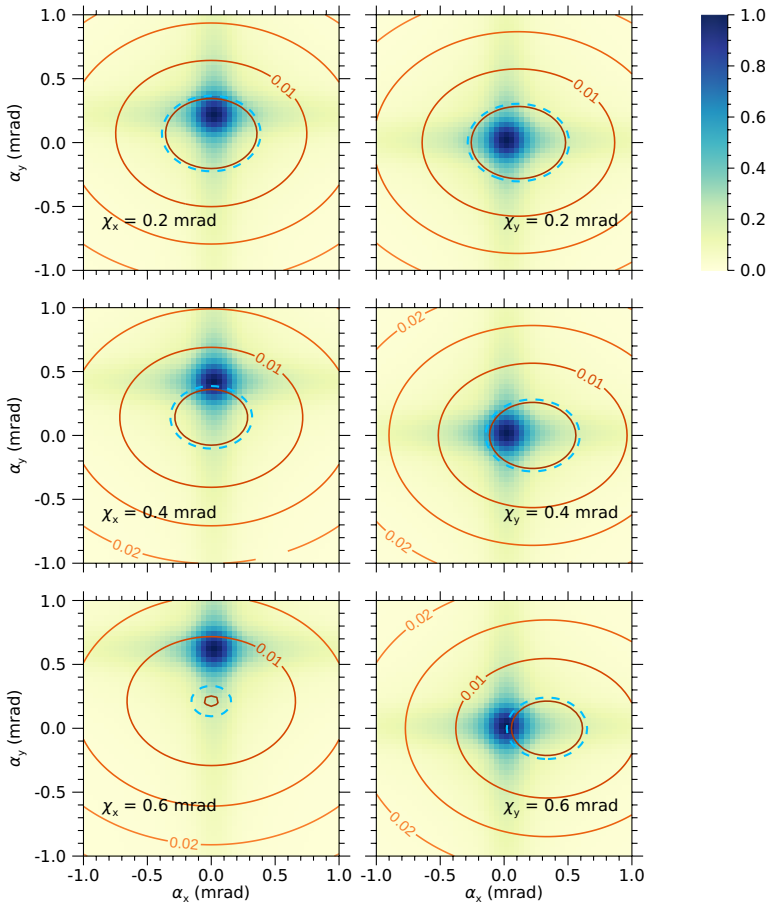

Figure 13. Field maps (in false colour) of the transmission of a system of misaligned crossed flat MLLs of NA = 0.0375 and focal lengths $f_1 = 1.25\,\mathrm{mm}$ and $f_2 = 1\,\mathrm{mm}$, for various rotations χ_x and χ_y of the first lens relative to the second. Contour maps of the RMS aberrations are superimposed, with the Marechal condition indicated by the dashed sky-blue line.

The imaging performance depends both on the wavefront aberration and the apodisation, as is visualised in figure 14 for a particular misalignment of two flat lenses with $\chi_x = 0.4\,\mathrm{mrad}$ and $\chi_y = 0.4\,\mathrm{mrad}$, compensated by a phase plate. The phase plate is assumed to conjugate the wavefront of perfectly-aligned lenses. The complex-valued pupil functions were constructed from the phase as given by the OPD and the amplitude equal to the square root of the transmission, plotted in the figure over a range of field angles α_x and α_y. As expected from figure 13 the field position that gives maximum transmission, at $(\alpha_x, \alpha_y) = (0, 0.2)\,\mathrm{mrad}$ does not correspond to the location of lowest aberration at $(\alpha_x, \alpha_y) = (0.1, 0.1)\,\mathrm{mrad}$. The wavefront at the location with maximum transmission is dominated by a 45° coma. The width of the apodised PSF at $(\alpha_x, \alpha_y) = (0.1, 0.1)\,\mathrm{mrad}$ is similar to that of the aberrated PSF at $(\alpha_x, \alpha_y) = (0, 0.2)\,\mathrm{mrad}$. Further from these field points, the PSF is dominated by the severe loss of diffraction efficiency at the edges of the pupil.

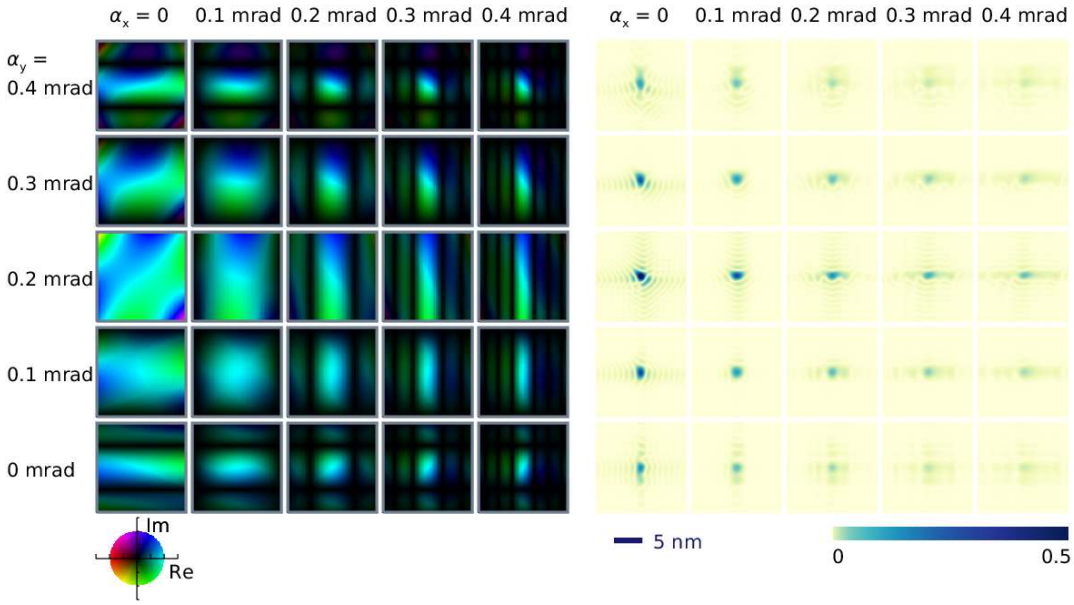

Figure 14. Complex-valued pupil functions and PSFs for a misaligned pair of 1D MLLs with NA = 0.0375 and focal lengths $f_1 = 1.25\,\mathrm{mm}$ and $f_2 = 1\,\mathrm{mm}$, for a range of field angles as indicated by α_x and α_y. The first lens is rotated by $\chi_x = 0.4\,\mathrm{mrad}$ and $\chi_y = 0.4\,\mathrm{mrad}$ relative to the second. The complex values of the pupil function are visualised by hue (phase) and brightness (amplitude) according to the colour wheel at bottom left. The corresponding PSFs are shown on a common intensity scale, which is truncated to a value of 0.5, compared with an intensity of 1 for a PSF of a lens with full amplitude and zero aberration.

6. Aberrations of imperfect multilayer Laue lenses

Imperfections of MLLs may include an error of the layer period d at a particular position of the lens, or an incorrect dependence of this period on position. The most trivial of these is a scaling of the lens, perhaps due to incorrect deposition rates, but a more problematic case is the variation of the deposition rate over the course of its fabrication. Other errors may be introduced by slicing the lens with an angular mis-cut, or by not achieving the necessary tilt of the layers in the deposition. Here we consider some of these cases to understand the tolerances required to make diffraction-limited MLLs.

6.1. Scale error of the MLL

An overall scaling of the MLL structure by a factor h may occur due to an error in the deposition rate used to make it. The dilation of the structure gives rise to a phase $\phi_m(r) = \phi(r/h)$ (of the "manufactured" lens in terms of the designed lens) which, from a Taylor expansion based on (3), yields a lowest-order term equal to $r^2/(2fh^2)$. The scaled MLL therefore has a focal length $f\,h^2$. The scale error places the n^{th} layer at hr_n, or at the position $r_{n(m)}$ given by $r_{n(m)}/h = r_n$. Each layer provides an extra wavelength of path, with $\phi_m(hr_n) = \phi(r_n) = n\lambda$. The scaling changes the spacings of the layers and

hence also the deflection angles of rays. Since $\partial\phi(r/h)/\partial r = \phi'(r/h)/h$, it follows from (5) that the periods of the scaled MLL are given by $hd(r/h)$ (for the case of the flat lens). That is, the period of the relocated n^{th} layer is scaled by h. From (6), this again shows that the focal length becomes $h^2 f$. The scaling also has an effect on higher-order aberrations. One way to conceptualise this case is to consider that scaling the lens and the wavelength by h similarly scales the focal length, as well as the OPD (in normalised pupil coordinates), by the same factor. That is, the spherical aberration of the scaled lens will be zero for a wavelength $h\lambda$. Reverting to the original wavelength will require scaling that by $1/h$ (giving a focal length h times larger again), and will be akin to the discussion of chromatic aberrations described in section 4.2, where now $\Delta\lambda/\lambda = 1/h - 1$. That is, for an axi-symmetric lens originally designed with focal length f and radius R, the spherical aberration of the scaled lens at the original design wavelength will be

$$\mathrm{OPD}_{\mathrm{SA}}(\rho; h) = \frac{3f}{8}\frac{1-h}{h}\left(1 + \frac{1}{h} - \frac{2f}{R}\right)\rho^4. \tag{32}$$

As with the chromatic aberration, the highest tolerance to scaling errors is achieved for $R = f$, but the allowable scaling error is limited primarily by violating the Bragg condition in the outermost layers, assuming that the layer tilts are also scaled (that is, that the entire lens structure is dilated uniformly in all directions). For the lens parameters and wavelength considered in section 4.3, a scaling error of less than about 1 % can be tolerated, as indicated by figure 5 (b).

6.2. Deposition rate stability

A drift in the rate of deposition of materials in the fabrication of an MLL will lead to an error in the d spacing and the position of those layers. Consider a deposition recipe that assumes a constant rate p of the accumulation of material which requires the material pairs to be alternated at deposition times T_n such that $r_n = pT_n$. However, if that rate changes in time then those layers will occur at positions

$$r_{n(m)} = \int_0^{T_n} p(1 + c(t))\,\mathrm{d}t. \tag{33}$$

A linear drift, $c(t) = c_1 t$, deposits layers according to $r_{n(m)} = pT_n + (c_1/2)pT_n^2 = r_n + (\beta/2)r_n^2$, where $\beta = c_1/p$ is the relative change in deposited thickness per thickness of material deposited (with units of inverse length). This coordinate error can be compared with the simpler scale error of section 6.1, showing that

$$\begin{aligned}\frac{\lambda}{2\pi}\phi_m(r) &= \frac{\lambda}{2\pi}\phi(r - \beta r^2/2) \\ &= s(r - \beta r^2/2) + \sqrt{(r - \beta r^2/2)^2 + (f - s(r - \beta r^2/2))^2} - f \\ &\approx \frac{r^2}{2f} - \frac{\beta r^3}{2f} + \left(\frac{2}{R} - \frac{1}{f}\right)\frac{r^4}{8f^2}.\end{aligned} \tag{34}$$

Here the inverse of the coordinate error was determined by solving $r_n + \beta r_n^2/2 = r_{n(m)}$ for r_n. When β is positive, the number of periods deposited over a height r is reduced, and so $\phi_m(r) < \phi(r)$ in agreement with (34).

As with off-axis aberrations of ideal (non-distorted) lenses, the incident beam impinging on the structure described by (34) no longer matches a reference beam that would give rise to a hologram described by ϕ_m, and accordingly the Bragg diffraction is modified due to the change in d spacing. The OPD must therefore be calculated according to (19), with a modified form of $\boldsymbol{q}$. In particular, since from (34) $\partial\phi_m(r)/\partial r = (1-\beta r)\,\phi'(r-\beta r^2/2)$, (16) must be replaced by $(1-\beta r)\,\boldsymbol{q}(r-\beta r^2/2)$. Analogously to the scaling error above, the period of the layer at r is modified by a multiplicative factor $1/(1-\beta r) \approx 1+\beta r$ and repositioned to $r_n + \beta r_n^2/2$. We find for the on-axis field point of a curved axi-symmetric lens,

$$\mathrm{OPD}(\rho) \approx -\beta f^2 \rho^3, \tag{35}$$

for the normalised pupil coordinate $\rho = r/f$. For a 1D lens, a similar scaling as for $\boldsymbol{q}$ must be applied to $\boldsymbol{q}_1$ in table 2. In this case we obtain the same result as (35) but with ρ replaced by the linear coordinate ρ_x or ρ_y.

Equation (35) shows that a linear drift of the deposition leads to a third-order error. For an axi-symmetric lens this is not coma (which has a direction and is not radial) and is a phase error that is approximately constant across the field. For a 1D lens, this does vary in a single direction as per the the coma terms proportional to ρ_x^3 and ρ_y^3 in (29). Thus, in that case, a small degree of deposition drift β can be compensated by tilting the lens, such that $(f_1/R_1 - 1)\alpha_y = \beta f_1$ (for $f_1 \neq R_1$). This compensation is only practical for field angles α_y that are smaller than the Darwin-width acceptance w_θ of the finest layers, which considerably limits the range of β that can be compensated. The RMS OPD error for a 1D lens with coma given by (35) is equal to $\beta f^2 \mathrm{NA}^3/(6\sqrt{7})$, minimised here by a defocus. The Marechal condition is satisfied when the RMS OPD is less than $\lambda/14$, and so without any compensation, we require

$$\beta < 1.13\lambda/(f^2\mathrm{NA}^3) \approx 9\delta/D^2 \tag{36}$$

where $\delta = \lambda/(2\mathrm{NA})$ is the lens resolution and $D = 2\mathrm{NA}f$ is the lens diameter. For $f = 1\,\mathrm{mm}$, $\mathrm{NA} = 0.037$, and $\lambda = 0.075\,\mathrm{nm}$, $\beta < 1.6\times10^{-6}\,\mu\mathrm{m}^{-1}$ or a relative error of 1.5×10^{-4} over the course of the entire deposition. This corresponds to an absolute error of 7.1 nm in the height of the lens.

Another example of a deposition error is a constant offset of the period, $d_m(r) = d(r) + \Delta d$. This can occur if the materials used to form the layers interdiffuse and create a thin interface with a different density to either of the unmixed materials [38]. It can be seen that this is in fact equivalent to the example just considered, since we have from (6) that $d(r) + \Delta d \approx \lambda f/r\,(1 + \Delta d\, r/(\lambda f))$, so that $\beta = \Delta d/(\lambda f)$. The magnitude of the coma generated by a given contraction error Δd increases as the wavelength is reduced, but from (36) a reduction in the focal length and the size of the lens relaxes the tolerance of Δd.

6.3. MLLs cut at an inclination

Multilayer Laue lenses are usually sliced to the desired thickness τ from an extended structure formed by material deposition. The angle at which a flat lens is cut might

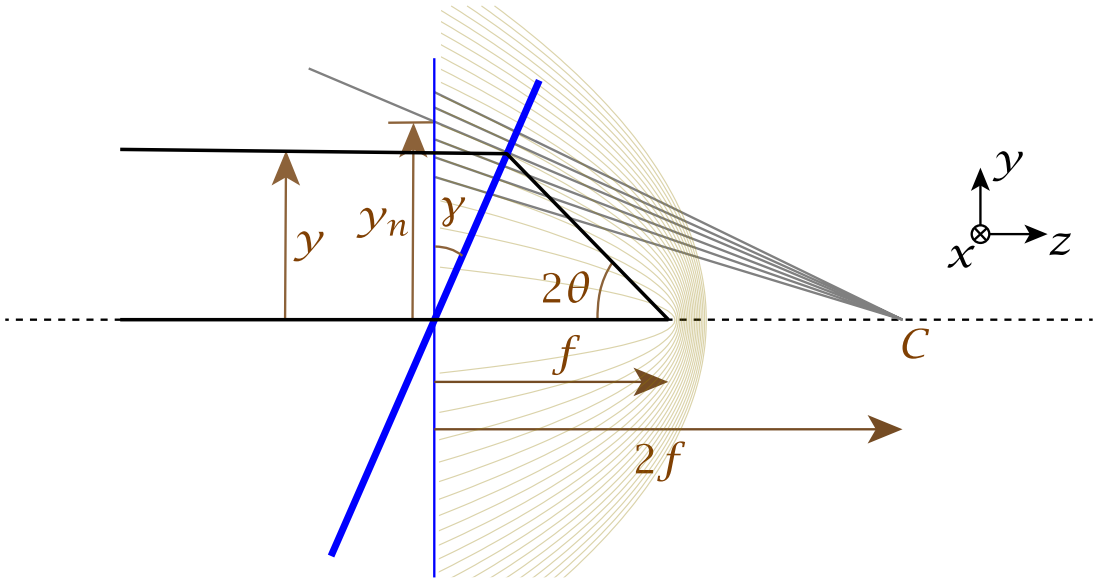

Figure 15. Geometry of a flat MLL of focal length f, cut at an incline with an angle γ. If the layers of the parent structure follow paraboloids (shown in brown) then rays (black lines) from an on-axis field angle will be focused without aberration. Flat tilted layers (shown in grey) will cause aberrations for the on-axis field angle.

not be exactly normal to the optic axis, or the center of curvature of a spherical surface might not exactly lie on that optic axis. We consider here the case of a flat lens cut at an angle that differs from the intended normal face by an angle γ. If the structure from which the lens is cut replicates the family of paraboloids that are described by (2), then the resulting optical element would be a tilted holographic lens, exhibiting zero OPD for the field point on the optical axis. Indeed, this will be the case for any arbitrary surface shape $z = s(r)$. Thus, in this case, cutting a lens at an incline will only change the off-axis aberrations. However, if the deposited layers only match the paraboloid forms on a particular surface (for example, $z = 0$) and differ in form away from that surface, then a mis-cut will cause an aberrated image of the on-axis field point. The aberration depends on the form of the layers at the positions cut by the surface, and we consider here the case of a flat 1D lens constructed from layers that are tilted planes.

We consider a lens that focuses in the y direction with a focal length f. The tilted planes of the structure from which the lens is sliced all intersect the optic axis a distance $2f$ from the lens vertex, as shown schematically in figure 15. The lens is cut on a plane that is tilted about the x axis by an angle γ, with the optic axis along z. A ray from the on-axis field angle intersects the lens at a height y and a longitudinal distance $z = y \tan\gamma$ from the vertex. The layer of the MLL intersected by this ray, which we presume to be the n^{th} period, passes through the $z = 0$ plane at a height $y_n = 2fy/(2f - y\tan\gamma)$. Since the lens was intended to be cut normal to the optic axis, the position y_n follows the prescription of (2) for $z = 0$. We see from figure 15 that for

positive γ the layers the ray intersects are thinner and placed closer to the optic axis than intended, but have almost the correct tilt to satisfy the Bragg condition. With analogy to the analysis in section 6.1 the lens can be considered to be locally scaled by the factor $y/y_n = 1 - y/(2f)\tan\gamma$ so that

$$\frac{\lambda}{2\pi}\phi_m(y) = \frac{\lambda}{2\pi}\phi\left(\frac{y}{1 - y/2f\tan\gamma}\right) = \sqrt{f^2 + \frac{y^2}{(1 - y/2f\tan\gamma)^2}}) - f. \quad (37)$$

Even though the surface of the MLL follows a tilted plane, we take $s(y) = 0$ in the derivation of $\phi_m(y)$ from (3) since the scaling accounts for this. Following the analyses of the previous sections,

$$\frac{\partial\phi_m(y)}{\partial y} = \frac{1}{(1 - y/2f\tan\gamma)^2}\phi'\left(\frac{y}{1 - y/2f\tan\gamma}\right), \quad (38)$$

and the expression for $\boldsymbol{q}(y)$ must be scaled in a similar way. The normal vector is

$$\hat{\boldsymbol{n}}(y) = (0,\, \sin\gamma, -\cos\gamma)\,. \quad (39)$$

For the on-axis field angle, we follow the ray-tracing procedure established in section 4 with $l_1 = y\tan\gamma$ and $l_2\,\hat{\boldsymbol{r}}'\cdot\hat{\boldsymbol{z}} = f - y\tan\gamma$. Using a symbolic mathematics program the Taylor expansion of the wavefront aberration is evaluated to

$$\mathrm{OPD}^{(4)}(\rho_y) = \frac{f}{2}\tan\gamma\,\rho_y^3 + \frac{f}{4}\tan^2\gamma\,\rho_y^4. \quad (40)$$

The dominating term is coma, proportional to ρ_y^3. This term depends linearly on the tangent of the mis-cut angle γ. To maintain the Marechal condition of an RMS wavefront error below $\lambda/14$ requires a mis-cut angle

$$\gamma < 2.3\frac{\lambda}{f\,\mathrm{NA}^3}, \quad (41)$$

or less than 3.3 mrad for the 0.0375 NA lens considered in section 5.4.

Perhaps more importantly, the linear dependence of coma on the mis-cut angle gives a way to easily compensate for the main component of drift in the deposition rate as explored in section 6.2. The coma error of (35) can be removed by cutting the lens at an angle given by $\tan\gamma = 2\beta f$. Setting a limit of $\tan\gamma < 1$ to ensure that the additional spherical aberration term of (40) is kept manageable, the largest drift in the deposition rate that can be tolerated is raised to $\beta = 1/(2f)$. For a lens with $f = 1\,\mathrm{mm}$, this corresponds to $5\times10^{-4}\,\mu\mathrm{m}^{-1}$ or a relative error of 3.75 % over the height of a 75 µm diameter lens. The range of angles at which the lens can be cut may be limited by satisfying the Bragg condition. The series expansion of the expression of the deviation parameter determined by solving $|\boldsymbol{r}'| = 1$ in the ray-trace procedure is given by

$$\epsilon = \frac{\tan\gamma}{2\cos\gamma}\rho^3 + \frac{7\tan^2\gamma}{8\cos\gamma}\rho^4. \quad (42)$$

Maintaining Bragg efficiency at the edge of the lens ($\rho = \mathrm{NA}$) therefore requires

$$\gamma < \frac{4|\delta_1 - \delta_2|}{\pi}\frac{1}{\mathrm{NA}^3}. \quad (43)$$

For the materials and parameters of the lens considered in section 5, the largest tolerable cut angle is thus about 160 mrad, which then limits the correctable deposition drift to no more than $0.8 \times 10^{-4}\,\mu\text{m}^{-1}$.

7. Discussion

The ray-tracing analyses of MLLs presented here, following procedures established for the design and characterisation of holographic optical elements, can be used as a guide for the design and manufacture of X-ray lenses by providing expressions for wavefront aberration maps of flat and curved MLLs formed from axi-symmetric or linear multilayer structures. These expressions further allow an understanding of the tolerances required to fabricate such lenses and the sizes of aplanatic areas of their image fields, as needed to design full-field or scanning microscopes. They also give insights into the potential capabilities of MLLs. As an example, we examined lenses of 1 mm focal length that give 1 nm resolution at a wavelength of 0.075 nm. The necessary tolerances to achieve diffraction-limited imaging (defined here as reaching a Strehl ratio of 0.8) are quite stringent, as would be expected in attempting to reach an RMS wavefront aberration of less than 0.005 nm. Any drift of the deposition rate when fabricating the layered structure must remain below a relative error of 1.5×10^{-4}, for example, although errors about 50 times this amount can potentially be compensated by an appropriate slicing of the lens from the structure at an angle (depending on details of the shape of the layers in the parent structure).

The question of alignment of MLLs in their use in high-magnification full-field or scanning microscopes comes down to the size of the aplanatic area of the image field of the lens. For our example cases for 1 nm imaging, the maximum field angle for diffraction-limited performance is about 1 mrad for a flat axi-symmetric lens, which can be increased by a factor of six by using the aplanatic zone-plate design on a sphere of radius equal to the focal length. In this lens, the range of field angles is limited by the ± 0.3 mrad acceptance of the Bragg reflection of the finest layers, so cutting the lens to a spherical shape might not be that beneficial. However, for lenses of longer focal length, the analytical expressions of the aberrations indicate that the aplanatic radius decreases with field angle, whereas the Bragg acceptance does not. Thus, for centimeter focal lengths there would be an advantage to a curved MLL. We note that curved lenses require that the layers are deposited to produce paraboloid surfaces, at least in the volume of the structure intersected by the spherical shape of the final lens.

Unlike thin zone plates which can be used over a large range of wavelengths limited by spherical aberration (but with a narrow bandwidth for any given choice of wavelength), thick MLLs of reasonably high NA can only be used over a narrow range of wavelengths that are limited by the acceptance of Bragg diffraction. This range depends inversely on the square of the NA and for 1 nm focusing at a wavelength of 0.075 nm with SiC/WC multilayers, this range is $\pm 0.6\,\%$. The range does not depend on focal length, and so any MLL design that achieves this resolution is limited to this wavelength

range. Other wavelengths require require different tilts of the layers.

Most MLLs made to date are linear structures that focus only in one dimension, as a cylindrical lens, and which are combined as a crossed pair to provide two-dimensional imaging. While they are easier to fabricate than axi-symmetric lenses, a crossed pair does suffer from a lower overall transmission than a single lens and cannot realise a completely null wavefront aberration. Even when perfectly aligned, the rays from an on-axis field point that are deflected by the first lens will not exactly match the Bragg condition in the second lens as required to create a perfect spherical converging wave. Overcoming this requires a second lens with layers that have a component of their tilt in the non-focusing direction. A pair of perfect crossed 1D MLLs gives rise to an aberration on axis proportional to the product of the squares of the pupil coordinate in each direction, which we refer to as an oblique spherical aberration, with a minimum RMS wavefront aberration equal to $0.08 f\,\mathrm{NA}^4$ for a focal length f. Diffraction-limited imaging, in which this RMS aberration is smaller than $\lambda/14$ is therefore only possible for crossed 1D MLLs of NA < 0.016 for focal lengths of 1 mm or more. However, this aberration could be overcome in higher NA lens pairs by conjugating the wavefront using a refractive phase plate, giving an aplanatic area similar to achievable in an axi-symmetric MLL. We also find that apodisation caused by this effect limits the highest NA of a lens system to a value that only depends on the rocking-curve width of the multilayer system. For the SiC/WC system considered here, this limit is NA $= 0.064$.

Crossed lenses pose more difficulty for alignment than axi-symmetric lenses where the aplanatic field simply tracks the region of the field that gives high diffraction efficiency. With crossed 1D MLLs, it is possible to tilt the lenses in such a way that the maximum diffraction efficiency does not match the region of diffraction-limited imaging. In practice, the alignment of such lenses may require wavefront sensing (such as speckle tracking [39]) to optimise the aberration and transmission as the relative tilts of the lenses are varied.

The analysis presented here generally assumed on-axis lenses where the optic axis passes through the center of the lens, but most 1D MLLs are constructed as off-axis portions of such a lens with the optic axis outside of the lens pupil. This does not change the conclusions of the dependence of aberrations on parameters such as NA and focal length since such lenses can be thought of as on-axis lenses with an additional phase tilt. Where there is a difference is in the acceptance widths of Bragg layers. For a given NA, the layer periods are obviously thinner for an off-axis lens than for the on-axis version, and these will have a narrower acceptance which will further restrict the field of view due to vignetting. This acceptance angle decreases linearly with pupil coordinate, so the field size of a lens for which the aperture ranges from 0 to D will be half of that which ranges from $-D/2$ to $D/2$, for the same numerical aperture.

The analysis presented here shows that producing MLLs at a resolution of 1 nm is not necessarily a challenge of making bigger lenses with more layers than currently demonstrated or in achieving higher accuracy in the deposition of those layers, but which could be addressed by a judicious choice of lens parameters such as focal

length and assessing and compensating for errors that might be introduced in lens manufacture. The old adage of optical fabrication is that you cannot make what you cannot measure. With accurate metrology of lens aberrations, the analytical methods presented, combined with an expanded design space that includes curving the lenses and ways to make corrections of lenses, it is hoped that X-ray imaging at 1 nm resolution will soon be realised.

Acknowledgments

This work was supported by the Cluster of Excellence "CUI: Advanced Imaging of Matter" of the Deutsche Forschungsgemeinschaft (DFG) - EXC 2056 - project ID 390715994.

References

[1] Yan H, Conley R, Bouet N and Chu Y S 2014 *J. Phys. D* **47** 263001
[2] Yan H, Kang H C, Conley R, Liu C, Macrander A T, Stephenson G B and Maser J 2010 *X-Ray Opt. Instrum.* **2010** 401854
[3] Bionta R M, Skulina K M and Weinberg J 1994 *Appl. Phys. Lett.* **64** 945–947
[4] Döring F, Robisch A, Eberl C, Osterhoff M, Ruhlandt A, Liese T, Schlenkrich F, Hoffmann S, Bartels M, Salditt T and Krebs H 2013 *Opt. Express* **21** 19311–19323
[5] Bajt S, Prasciolu M, Fleckenstein H, Domaracký M, Chapman H N, Morgan A J, Yefanov O, Messerschmidt M, Du Y, Murray K T, Mariani V, Kuhn M, Aplin S, Pande K, Villanueva-Perez P, Stachnik K, Chen J P J, Andrejczuk A, Meents A, Burkhardt A, Pennicard D, Huang X, Yan H, Nazaretski E, Chu Y S and Hamm C E 2018 *Light: Sci. Appl.* **7** 17162
[6] Maser J and Schmahl G 1992 *Opt. Comm.* **89** 355–362
[7] Yan H, Maser J, Macrander A, Shen Q, Vogt S, Stephenson G B and Kang H C 2007 *Phys. Rev. B* **76** 115438
[8] Hu L, Chang G, Liu P and Zhou L 2015 *J. Synchr. Rad.* **22** 936–945
[9] Yan H, Huang X, Bouet N, Zhou J, Nazaretski E and Chu Y S 2017 *Opt. Express* **25** 25234–25242
[10] Ali S and Jacobsen C 2020 *J. Opt. Soc. Am. A* **37** 374–383
[11] Murty M V R K 1960 *J. Opt. Soc. Am.* **50** 923–923
[12] Young M 1972 *J. Opt. Soc. Am.* **62** 972–976
[13] Welford W 1973 *Optics Comm.* **9** 268–269
[14] Hetirick M C 1986 *Appl. Opt.* **25** 3269–3282
[15] Latta J N 1971 *Appl. Opt.* **10** 2698–2710
[16] Close D H 1975 *Opt. Eng.* **14** 408–419
[17] Welford W 1975 *Optics Comm.* **14** 322–323
[18] Welford W T 1986 *Aberrations of optical systems* (Bristol, England: IOP Publishing)
[19] Fairchild R C and Fienup J R 1982 *Opt. Eng.* **21** 133–140
[20] Lindlein N and Schwider J 1992 *J. Euro. Opt. Soc. A* **1** 111–125
[21] Klein A 2008 *J. Opt. Soc. Am. A* **25** 979–982
[22] Yu N, Genevet P, Kats M A, Aieta F, Tetienne J P, Capasso F and Gaburro Z 2011 *Science* **334** 333–337
[23] Aieta F, Genevet P, Kats M and Capasso F 2013 *Opt. Express* **21** 31530–31539
[24] Windt D L, Donguy S, Hailey C J, Koglin J, Honkimaki V, Ziegler E, Christensen F E, Chen H, Harrison F A and Craig W W 2003 *Appl. Opt.* **42** 2415–2421
[25] Prasciolu M, Leontowich A F G, Krzywinski J, Andrejczuk A, Chapman H N and Bajt S 2015 *Opt. Mater. Express* **5** 748–755

[26] Li K, Wojcik M and Jacobsen C 2017 *Opt. Express* **25** 1831–1846
[27] Authier A 2001 *Dynamical Theory of X-Ray Diffraction* (Oxford University Press)
[28] Goodman J W 1996 *Introduction to Fourier Optics, Second Edition* (McGraw-Hill)
[29] Born M and Wolf E 2002 *Principles of Optics* 7th ed (Cambridge University Press)
[30] Kogelnik H 1969 *Bell System Technical Journal* **48** 2909–2947
[31] Bajt S, Chapman H N, Aquila A and Gullikson E 2012 *J. Opt. Soc. Am. A* **29** 216–230
[32] Bokor N and Davidson N 2001 *Appl. Opt.* **40** 5825–5829
[33] Murray K T, Pedersen A F, Mohacsi I, Detlefs C, Morgan A J, Prasciolu M, Yildirim C, Simons H, Jakobsen A C, Chapman H N, Poulsen H F and Bajt S 2019 *Opt. Express* **27** 7120–7138
[34] Cowley J M 1981 *Diffraction Physics* (North-Holland)
[35] Yuan S and Sasian J 2009 *Appl. Opt.* **48** 2574–2584
[36] Seiboth F, Schropp A, Scholz M, Wittwer F, Rödel C, Wünsche M, Ullsperger T, Nolte S, Rahomäki J, Parfeniukas K, Giakoumidis S, Vogt U, Wagner U, Rau C, Boesenberg U, Garrevoet J, Falkenberg G, Galtier E C, Ja Lee H, Nagler B and Schroer C G 2017 *Nature Comm.* **8** 14623
[37] Jenkins F A and White H E 1976 *Fundamentals of Optics* (New York: McGraw-Hill) chap 10.20 4th ed
[38] Petford-Long A K, Stearns M B, Chang C, Nutt S R, Stearns D G, Ceglio N M and Hawryluk A M 1987 *J. Appl. Phys.* **61** 1422–1428
[39] Zdora M C 2018 *J. Imaging* **4**